Tectonics

RESEARCH ARTICLE
10.1029/2021TC006846

Key Points:

- We estimate 9.1 ± 1.3 mm/yr of right-lateral strike-slip on the Main Köpetdag fault, Turkmenistan
- The presently active tectonics likely dates from 3 to 5 Ma, assuming that there has been ~35 km of strike-slip displacement across the fault
- The South Caspian moves relative to Iran and Eurasia, with the latter being at a rate of 10.4 ± 1.1 mm/yr in direction 333° ± 5

Correspondence to:

R. T. Walker,
richard.walker@earth.ox.ac.uk

Citation:

Walker, R. T., Bezmenov, Y., Begenjev, G., Carolin, S., Dodds, N., Gruetzner, C., et al. (2021). Slip-rate on the Main Köpetdag (Kopeh Dagh) strike-slip fault, Turkmenistan, and the active tectonics of the South Caspian. *Tectonics*, *40*, e2021TC006846. https://doi.org/10.1029/2021TC006846

Received 30 MAR 2021
Accepted 8 JUL 2021

Slip-Rate on the Main Köpetdag (Kopeh Dagh) Strike-Slip Fault, Turkmenistan, and the Active Tectonics of the South Caspian

R. T. Walker[1], Y. Bezmenov[2], G. Begenjev[2], S. Carolin[1,3], N. Dodds[1], C. Gruetzner[4,5], J. A. Jackson[4], R. Mirzin[2], Z. Mousavi[6], and E. J. Rhodes[7,8]

[1]Department of Earth Sciences, COMET, Oxford University, Oxford, UK, [2]Institute of Seismology and Physics of the Atmosphere, National Academy of Sciences of Turkmenistan, Aşgabat, Turkmenistan, [3]Department of Earth Sciences, University of Cambridge, Cambridge, UK, [4]Department of Earth Sciences, Bullard Laboratories, University of Cambridge, Cambridge, UK, [5]Friedrich Schiller University Jena, Institute of Geological Sciences, Jena, Germany, [6]Department of Earth Sciences, Institute for Advanced Studies in Basic Sciences, Zanjan, Iran, [7]Department of Geography, University of Sheffield, Sheffield, UK, [8]Department of Earth, Planetary, and Space Sciences, University of California Los Angeles, Los Angeles, CA, USA

Abstract We provide the first measurement of strike-slip and shortening rates across the 200-km-long right-lateral strike-slip Main Köpetdag Fault (MKDF) in Turkmenistan. Strike-slip and shortening components are accommodated on parallel structures separated by ~10 km. Using Infra-red-stimulated luminescence and reconstruction of offset alluvial fans we find a right-lateral rate of 9.1 ± 1.3 mm/yr averaged over 100 ± 5 ka, and a shortening rate of only ~0.3 mm/yr averaged over 35 ± 4 ka across the frontal thrust, though additional shortening is likely to be accommodated locally by folding and faulting, and regionally within the eastern Caspian lowlands to its south. The MKDF is estimated to have ~35 km of cumulative right-lateral slip which, if these geological measurements are correct, would accumulate in only 3–5 Ma at the rate we have determined, suggesting that the present tectonic configuration started within that time period. We use the MKDF slip-rate to form a velocity triangle, from which we estimate the Iran-South Caspian and Eurasia-South Caspian shortening rates, and show that the South Caspian Basin moves at 10.4 ± 1.1 mm/yr in direction 333° ± 5 relative to Eurasia and at 4.8 ± 0.8 mm/yr in direction 236° ± 14 relative to Iran. In contrast to both the eastern Köpetdag and the Caspian lowlands the MKDF has little recent or historical seismicity. The rapid slip-rate estimated here suggests that it is a zone of high earthquake hazard.

1. Introduction

Turkmenistan is situated at the northern edge of the belt of shortening related to the Arabia-Eurasia continental collision (Figure 1). Yet the active faulting within Turkmenistan is influenced both by Arabia-Eurasia plate convergence and by the motion of the South Caspian Basin (SCB), Figure 2a, which is an aseismic block that moves independently to its surroundings (e.g., Copley & Jackson, 2006; Djamour et al., 2010; Jackson et al., 2002). The directions, rates, and rotation poles of the SCB relative to Iran and Eurasia are not well resolved, thus limiting our understanding of the tectonic influence on the stratigraphy and evolution of the basin interior, and on the styles and rates of faulting around its margins.

The relative motion between the SCB and surrounding parts of NE Iran and Turkmenistan is partly accommodated by the Shahroud left-lateral fault zone (SFZ, Figure 2a) in Iran and the right-lateral Main Köpetdag fault (MKDF, Figure 2a) in Turkmenistan (e.g., Hollingsworth et al., 2006, 2008, 2010). (We use the spellings for geographical and town names as used in Turkmenistan, rather than the Persian equivalents as often used in papers describing the regional tectonics. Thus Köpetdag rather than Kopeh Dagh, Aşgabat rather than Ashkabad). Determining the slip-rates and cumulative displacements on these two fault zones is hence important for examining the tectonic evolution of the SCB (e.g., Hollingsworth et al., 2008). Measurements of strain accumulation across the SFZ from both InSAR and GPS are consistent and show 4.8 ± 0.8 mm/yr of left-lateral motion being stored across the fault (Mousavi et al., 2015). These present-day values are also consistent with late Quaternary rates of left-lateral faulting summed across the Abr and Khuj segments of the Shahroud fault (Javidfakhr et al., 2011). In contrast, the right-lateral slip-rate of the MKDF

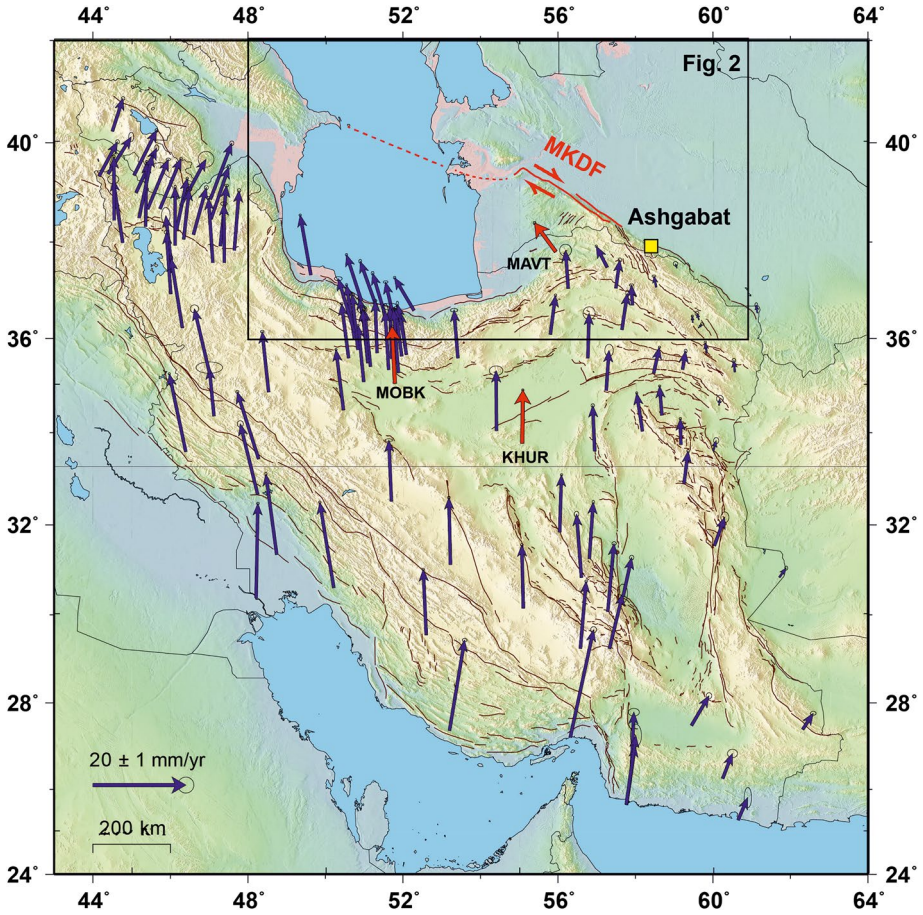

Figure 1. GPS velocities from permanent stations within Iran (selected from those presented in Khorrami et al. (2019). The permanent stations MOBK and KHUR, from which we estimate the shortening rate and direction between Iran and Eurasia are marked in red, as is the station MAVT in northeast Iran. The Main Köpetdag fault (MKDF) is labeled and marked in red. The box represents the region shown in Figure 2a. Latitudes and longitudes in this, and in all later maps, are in degrees north and east.

has proven difficult to constrain using geodetic methods. A pole of rotation for the SCB relative to Eurasia calculated from GPS measurements in northern Iran predicts a right-lateral rate of only ~3 mm/yr on the MKDF (Djamour et al., 2010). Alternatively, a faster slip-rate of 6.7 ± 0.5 mm/yr can be inferred from GPS by taking the fault parallel velocity of the two stations sited in the eastern Caspian lowlands, and assuming that all is accommodated across the MKDF (Mousavi et al., 2013). InSAR measurements of strain accumulation across the MKDF are contaminated by large changes in atmospheric conditions, giving a rate of strain accumulation anywhere in the range 5–12 mm/yr (Walters et al., 2013).

In this study, we present the initial findings of a joint Turkmenistan-UK project on the active tectonics of the territory of Turkmenistan. We provide the first estimate of late Quaternary slip-rate on the right-lateral MKDF, from the section between the towns of Serdar and Baharly (Figure 2b), by restorating the offset of displaced alluvial fans and by dating these fans using infra-red-stimulated luminescence dating. We then use our findings to further our understanding of the tectonics in this scientifically and economically important region. Destructive earthquakes have occurred within Turkmenistan, including the 1948 Ashagbat earthquake east of the MKDF, and the 1895 Krasnovodsk earthquake within the Caspian lowlands of Turkmenistan (Ambraseys, 1997, Figure 2a). However, there is little evidence for major earthquake rupture on the MKDF itself, either recently or historically (e.g., Ambraseys, 1997; Ambraseys & Melville, 2005; Berberian, 2014; Berberian & Yeats, 2001, see Figure 3), and so our measurement of its slip-rate is of importance in estimating the hazard that it poses.

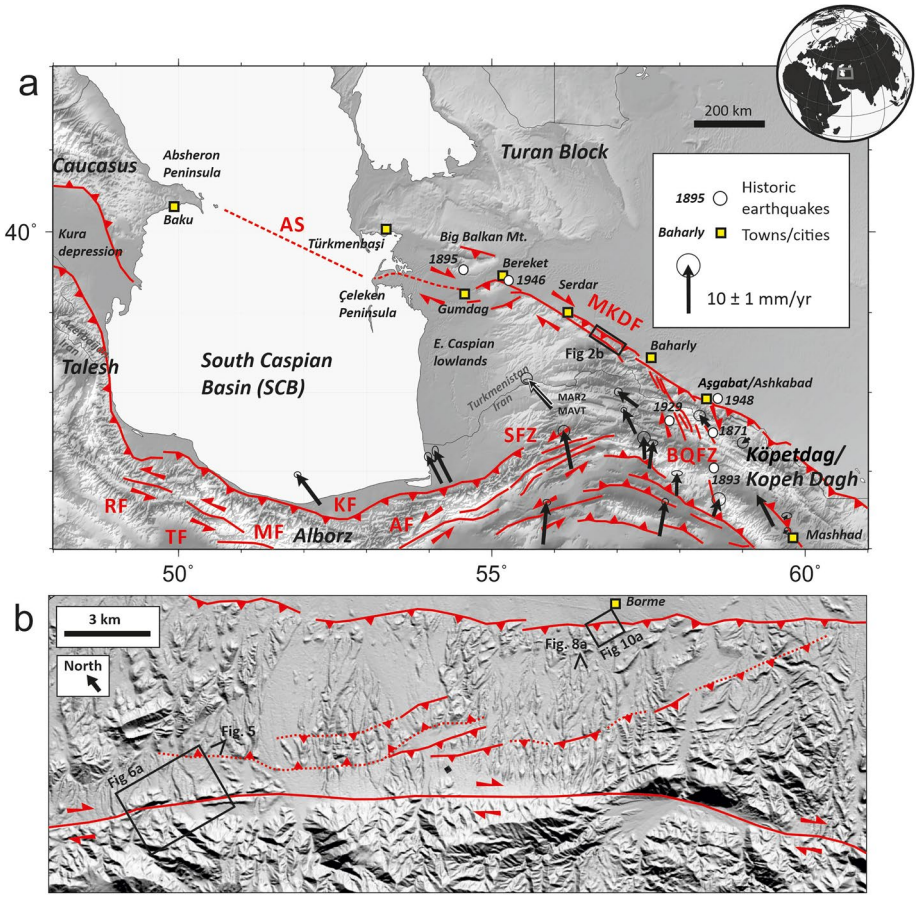

Figure 2. (a) Simplified active fault of the South Caspian region (MKDF = Main Köpetdag Fault, AS = Absheron Sill, SFZ = Shahrud Fault Zone, BQFZ = Barharden-Quchan Fault Zone). GPS velocities from NE Iran are from Mousavi et al. (2013). Historical earthquakes (Mw > 7) in Turkmenistan and adjacent parts of Iran are shown as white circles (from Ambraseys, 1997). Yellow squares represent towns. (b) Digital elevation model derived from stereo SPOT-6 satellite imagery. Active faults are marked by solid red lines where surface scarps are visible, and dotted where surface scarps are not identified. Reverse faults are annotated with teeth on their hanging-wall sides, and strike-slip faults annotated with paired opposing arrows. Parallel strike-slip and thrust faults are separated by ~7–10 km, which represents the hanging-wall of the thrust. The hanging-wall exposes folded Tertiary deposits that are incised into Badlands. Several late Quaternary scarps are present within the hanging-wall, indicating additional shortening away from the frontal thrust. A right-stepping en-echelon arrangement suggests that further diffuse right-lateral slip may occur.

2. Motion of the South Caspian Basin (SCB) Relative to Its Surroundings

The SCB may have originated in the Mesozoic as part of a wider back-arc basin (e.g., Cowgill et al., 2016; Mosar et al., 2010; Vincent et al., 2007). Up to 20 km of sediment has been deposited in the basin interior, of which half has accumulated within the last 5.5 Ma (e.g., Allen et al., 2002; Green et al., 2009; Robert et al., 2014). Earthquakes with depths down to 80 km occur in a narrow band north of the northern margin of the SCB (north of the Apsheron Sill, marked AS, Figure 3) and down to 40 km beneath the Talesh and Caucasus mountains at its western margin (Aziz Zanjani et al., 2013; Jackson et al., 2002, Figure 3, also see Appendix A). The deep earthquakes north of the Apsheron sill are thought to result from underthrusting and subduction of the SCB basement, with the onset of subduction often assumed to correlate with the increase in sediment accumulation at 5.5 Ma (e.g., Allen et al., 2002), though some authors argue that the sediment accumulation can be explained as the result of river incision, sediment deposition, and subsidence due to sediment loading following early Pliocene sea-level drawdown (Green et al., 2009) rather than purely by tectonically driven subsidence.

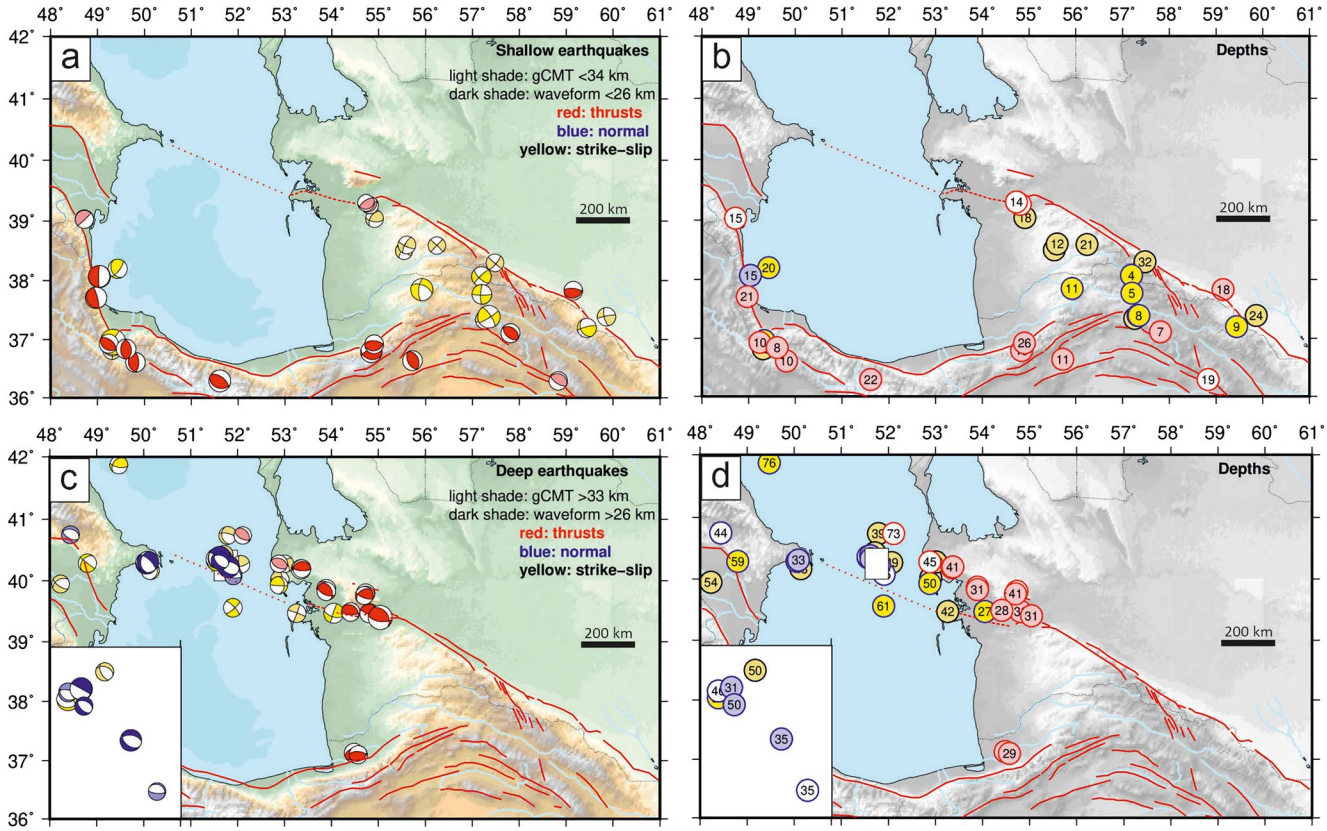

Figure 3. Instrumental earthquakes of the South Caspian and its surroundings, updated from Jackson et al. (2002). The additional mechanisms are listed in Appendix A. Red lines represent active fault locations. (a) Earthquakes with depths of less than 34 km from the global CMT catalog or 26 km or less from waveform modeling. The earthquakes are divided by color, with thrust mechanisms in red, normal in blue, and strike-slip in yellow. (b) The depths of shallow earthquakes as shown in panel "a", with color again representing mechanism type. (c) Earthquakes with depths of more than 33 km from the global CMT catalog or more than 26 km from waveform modeling. The inset, bottom left, shows the closely spaced earthquakes from the mid-Caspian. (d) Depths of deep earthquakes as shown in panel "c".

East of the Caspian, the MKDF runs along the Köpetdag range, which expose a sequence of lithologies ranging from Jurassic to Quaternary in age (e.g., Ghassemi & Garzanti, 2019; Robert et al., 2014), which have been folded and deformed during several tectonic phases. Following the Cimmerian orogeny, a period of rifting oriented parallel to the older Paleotethys suture began in the mid Jurassic. Up to 7 km of mid-Jurassic to Tertiary sediments were deposited until a major phase of basin inversion and folding in the late Eocene (Robert et al., 2014). Jurassic deposits are exposed predominantly in the eastern parts of the range, with Cretaceous and Tertiary age deposits more common in the central and western parts. An onset of the present-day tectonic activity, involving oblique strike-slip and reverse motion within the Köpetdag and eastern Alborz ranges, has been proposed anywhere from ~10 Ma (e.g., Hollingsworth et al., 2008) to as recently as ~2 Ma (e.g., Ritz et al., 2006).

The right-lateral MKDF that now bounds the Köpetdag range and the left-lateral SFZ within the eastern Alborz are together thought to accommodate a WNW expulsion of the SCB (e.g., Hollingsworth et al., 2006, 2010). The MKDF and SFZ terminate eastwards at the NNW-SSE right-lateral faults of the Bar-harden-Quchan fault zone (BQFZ, Figure 2a), which cut through the Köpetdag range, and right-laterally displace anticlines in the Mesozoic and Tertiary bedrock, showing a change from shortening to strike-slip within this central part of the range (e.g., Hollingsworth et al., 2006). The BQFZ is likely to accommodate along-strike extension within the Köpetdag, as confirmed by recent GPS velocities (Mousavi et al., 2013), and separates the easternmost parts of the Köpetdag range that accommodate purely N-S Iran-Eurasia shortening, and in which Jurassic age rocks are exposed, from more westerly parts that are influenced by WNW expulsion of the SCB, and which expose predominantly Cretaceous and Tertiary rocks.

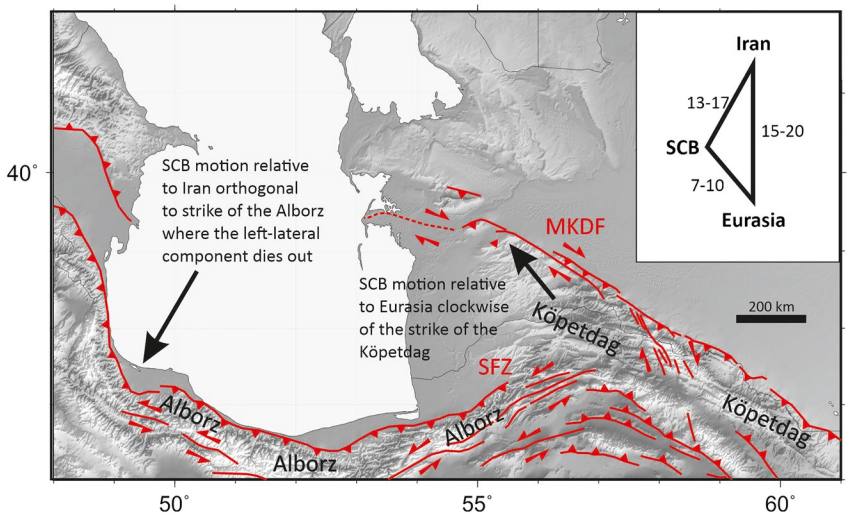

Figure 4. Construction of the velocity triangle in Jackson et al. (2002). Active faults are marked in red, with annotation as in Figure 2a. The motion of the SCB relative to Iran is likely to be orthogonal to the strike of the Alborz at the point where its component of left-lateral faulting dies away. The motion of the SCB relative to Eurasia must be clockwise of the strike of the MKDF, to reflect the right-lateral strike-slip and unknown amount of shortening across that range. Later GPS measurements have shown the rate of 15–20 mm/yr for the Iran-Eurasia shortening to be an overestimate. In this paper we use an updated GPS estimate of the Iran-Eurasia shortening, along with measurements of the strike-slip rates along the MKDF and SFZ, to estimate the amounts of South Caspian-Iran and South Caspian- Eurasia shortening, and to constrain the SCB motion relative to both Iran and Eurasia.

The available GPS measurements are confined to a narrow strip along the southern Caspian shore and a small number of stations in the folded terrain east of the Caspian (Figures 1 and 2a). All of these measurements are likely to be contaminated by strain accumulation near the basin margins, as suggested by earthquakes in the eastern Caspian lowlands (e.g., Nemati et al., 2013, Figure 3) and by the imaging of folds and thrusts within the thick sedimentary sequence of the eastern Caspian lowlands (e.g., Radfar et al., 2019). Djamour et al. (2010) produced a model of South Caspian motion relative to Eurasia by finding a best fit to the available GPS velocities, which indicated a clockwise rotation of the South Caspian region about a pole of rotation that is sited only a few hundred kilometres NE of the Caspian. In turn indicating a right-lateral slip-rate on the MKDF of only ~3 mm/yr, with a shortening component that varies along the fault length and comparable in magnitude to the strike-slip rate along its central section. Mousavi et al. (2013) instead extrapolate the velocities from stations MAR2 and MAVT stations (Figure 2a) to the MKDF, yielding a faster right-lateral strike-slip rate for the MKDF of 6.7 ± 0.5 mm/yr and shortening of 2.5 ± 1.0 mm/yr. Whether the rate from Mousavi et al. (2013) is representative of the SCB as a whole requires negligible deformation to occur within the region between the MKDF and SFZ, which might not be a valid assumption.

The variation in styles and rates of faulting around the SCB margins can be used to estimate the motion of the SCB relative to both Eurasia and to central Iran through the construction of a velocity triangle (Copley & Jackson, 2006; Jackson et al., 2002). As there is an unknown amount of deformation occurring across the Köpetdag and eastern Alborz, and also in the eastern Caspian lowlands between them, the trends of the range-parallel strike-slip faults within the SFZ and MKDF do not directly constrain the direction of motion of the SCB relative to Iran and Eurasia. Estimates have been made, however, based on the styles of faulting around the margins. An example, from Jackson et al. (2002), is shown on Figure 4. In the absence of GPS data, they used a value for the Iran-Eurasia shortening that is too high, and were limited by the lack of direct constraint on the rates of strike-slip within the Alborz and Köpetdag ranges. They estimate 7–10 mm/yr in a direction north of 300° for the motion of the SCB relative to Eurasia and 13–17 mm/yr in direction 210° relative to Iran. Copley and Jackson (2006), constructed velocity triangles to estimate a SCB-Eurasia motion of 11 ± 2 mm/yr in direction 335° ± 5 and a SCB-Iran motion of 7 ± 1 mm/yr in direction 225°.

In this paper we take advantage of improved measurements of Iran-Eurasia shortening from permanent GPS stations within Iran (Khorrami et al., 2019), along with direct measurements of range-parallel strike-slip

in the eastern Alborz (Mousavi et al., 2015) and Köpetdag (this paper), to provide better constraint on the motion of the SCB relative to both Iran and Eurasia. The approach that we take in constructing our velocity triangle allows us to estimate the amount of shortening perpendicular to the eastern Alborz and Köpetdag, and thus the overall motion of the SCB.

3. Geomorphology of the MKDF

The right-lateral MKDF runs for over 200 km along the northern margin of the Köpetdag mountain range between longitudes 55°E and 57.5°E, adjacent to Baharly and Bereket towns (Figure 2). East of Baharly the Köpetdag rangefront continues, but the absence of large lateral offsets in the geomorphology, combined with the presence of vertical scarps, suggests that the active faulting is predominantly reverse. West of Bereket faulting is hard to trace through the plains of the eastern Caspian lowlands. Active fault scarps are visible along the northern margin of the Big Balkan range, but some of the activity on the MKDF appears to shift southwestward to Gumdag, where a pair of strike-slip earthquakes occurred in 1983 and 1984 (Jackson et al., 2002). The right-lateral strike-slip system then appears to continue to the Caspian shore at the Çeleken peninsula, beneath a series of en-echelon anticlines (Van Dijk et al., 2018). Presumably the right-lateral strike-slip continues offshore, toward the Apsheron Sill in the Caspian interior (AS on Figure 2a), though it is not clear how closely the onshore and offshore faults are connected structurally (e.g., Jackson et al., 2002).

A shortening component of slip exists along the entire 200 km length of the MKDF between Baharly and Bereket, as evidenced by a vertical component of displacement in late Quaternary landforms, and by the longer-term development of the Köpetdag Mountains. For a distance of ~80 km eastwards from Serdar town, the dip-slip and strike-slip components of motion are accommodated on two parallel structures separated by 7–10 km orthogonal to strike. The parallel thrust and strike-slip faults of the MKDF are shown in detail in Figure 2b. Folding and faulting north of the strike-slip fault, within the hanging-wall of the thrust, indicates that a part of the shortening is accommodated within the hanging-wall. The right-stepping en-echelon arrangement of the hanging-wall structures might also suggest the presence of diffuse strike-slip motion. It is in this section of the MKDF, as shown in Figure 2b, that we estimate the rate of strike-slip and shortening across the fault zone.

3.1. Rate of Strike-Slip on the MKDF

In November 2016, a joint team of Turkmenistan and UK scientists visited the MKDF to provide estimates of the long-term slip-rate on the fault. We targeted the part of the fault shown in Figure 2b, where strike-slip and dip-slip components are separated onto sub-parallel structures at the surface. Large right-lateral cumulative displacements are seen along this section (Figures 2b and 5–7), and we consider it the most promising section for estimating the slip-rate of the fault, given that it becomes more diffuse toward both its eastern and western ends. To estimate the component of shortening we targeted the range-parallel reverse fault adjacent to a minor river cut close to the village of Borme (Figure 2b), where fresh cuttings through the gravel deposits outcrop in the channel margins (see Section 3.2).

Our strike-slip measurement site is shown in Figures 5 and 6a. Large alluvial fan systems have been deeply incised by rivers that record cumulative right-lateral displacements. Hollingsworth (2008) recognised that the rivers at our site, and others along a ~10-km-long stretch of the fault extending WNW from our study site, appear to record consistent displacements of ~900 m. We used Worldview-2 50 cm optical satellite imagery to provide a more detailed estimate of the offset. We then combine this estimate with constraint on the age of the fan in order to provide an estimate on slip rate.

In Figure 5, we show an oblique view of the MKDF looking west toward our study site. Southwest of the fault there is widespread exposure of bed rock, which is predominantly Mesozoic limestone. Northeast of the fault the topography is subdued, with large alluvial fans overlying folded and exhumed basin sediments of Tertiary age, though isolated outcrops of limestone form shutter ridges along the purely strike-slip fault, and also occur at a minor restraining bend. Northward-flowing river systems exit the bedrock exposures of the mountains and then incise into the fan surface. These rivers show apparent right-lateral deflections at the fault. We have labeled a series of five closely spaced rivers on the southwest side of the fault as A–E and a sixth as F. These six rivers appear to correlate with outlets on the other side of the fault,

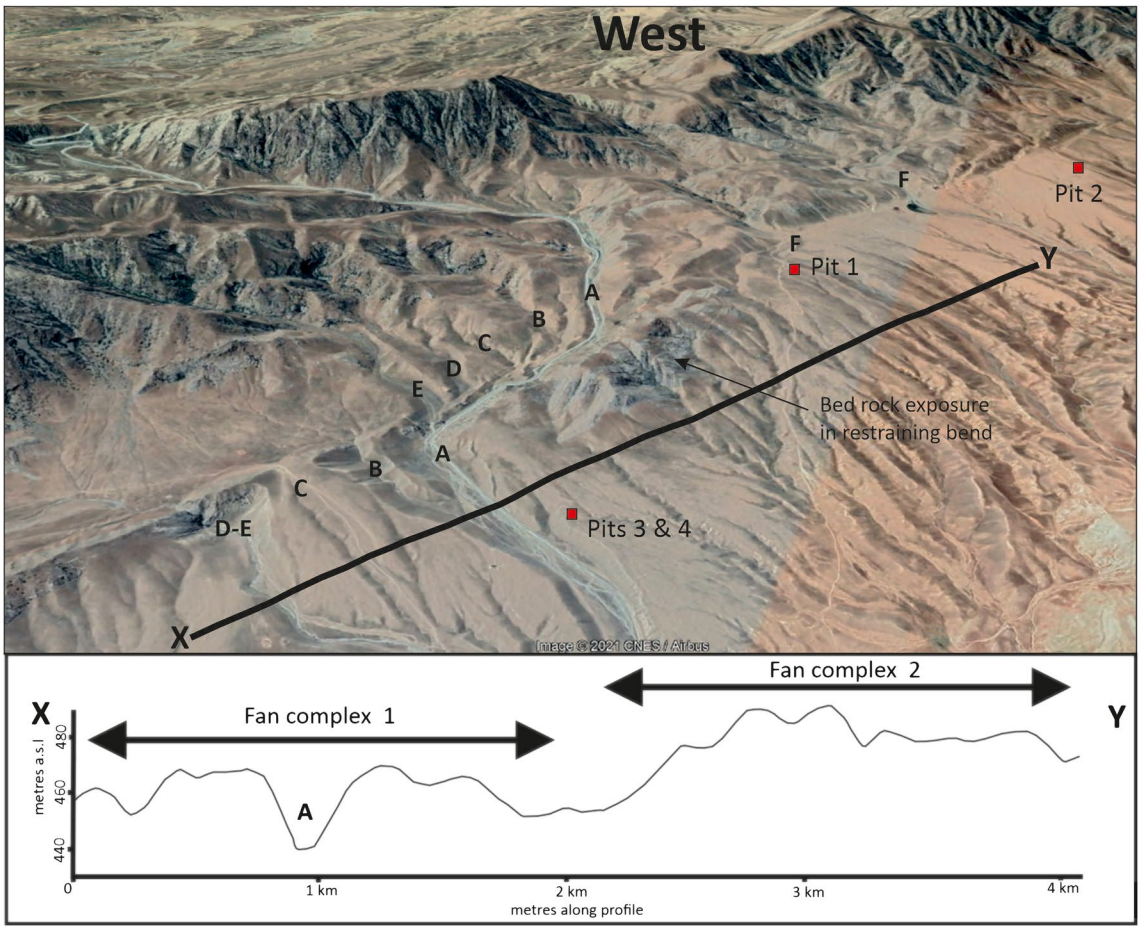

Figure 5. Perspective view of the sample sites along the Main Köpetdag strike-slip fault (see Figure 2b for location). The fault separates Mesozoic limestone bedrock exposures of the Köpetdag range (in the distance) from alluvial fans deposited over exhumed basin sediments (in the foreground). Five stream channels (A–E) on the upstream, far, side of the fault correspond to five channels on the downstream side and are restored with ~950 m of displacement (see Figure 6). A topographic profile along line X-Y is shown in the lower panel. Outlets A-E are all incised into the convex-up surface of a single fan complex. Pits 3 & 4 were excavated into this fan surface. Pit 1 was excavated into a separate fan complex, though the ~950 m offset of outlet F, along with the similarity in sample age between the samples from Pit 1 and Pits 3 & 4, lead us to suspect they are contemporaneous.

also labeled A–F, implying relatively large and consistent amounts of right-lateral deflections (e.g., Hollingsworth et al., 2008). A topographic profile drawn through the alluvial fans northeast of the fault (line X–Y on Figure 5) shows two convex-up surfaces, one corresponding to deposition associated with the five closely spaced rivers A–E, and the other corresponding to deposition from F. The elevations of these two fans, which are sourced from separate catchments, does not provide direct information on age, though their morphologies and the amount of displacement of streams within them suggest they are contemporaneous. Only this alluvial fan surface is observed, and there are no inset river terrace levels preserved where rivers have cut into it surface.

The closely spaced rivers A–E (Figure 5) are shown in detail in the satellite image in Figures 6a and 6b, we have annotated the image to show limits of bedrock exposure (purple), the extensive alluvial fan surface (orange), and the drainage network (blue). We have identified small remnants of alluvial surface on the southwest side of the fault, such that rivers A–E are incised into alluvium on both sides of the fault. We correlate these small fan remnants with the more extensive surface preserved to the northeast of the fault, based upon the degree of incision and color characteristics in the Worldview data. The surface can be distinguished from younger alluvial fan surfaces present on the southwest side of the fault as these younger surfaces are noticeably darker, with distributary channel networks that are more clearly defined (Figure 6b).

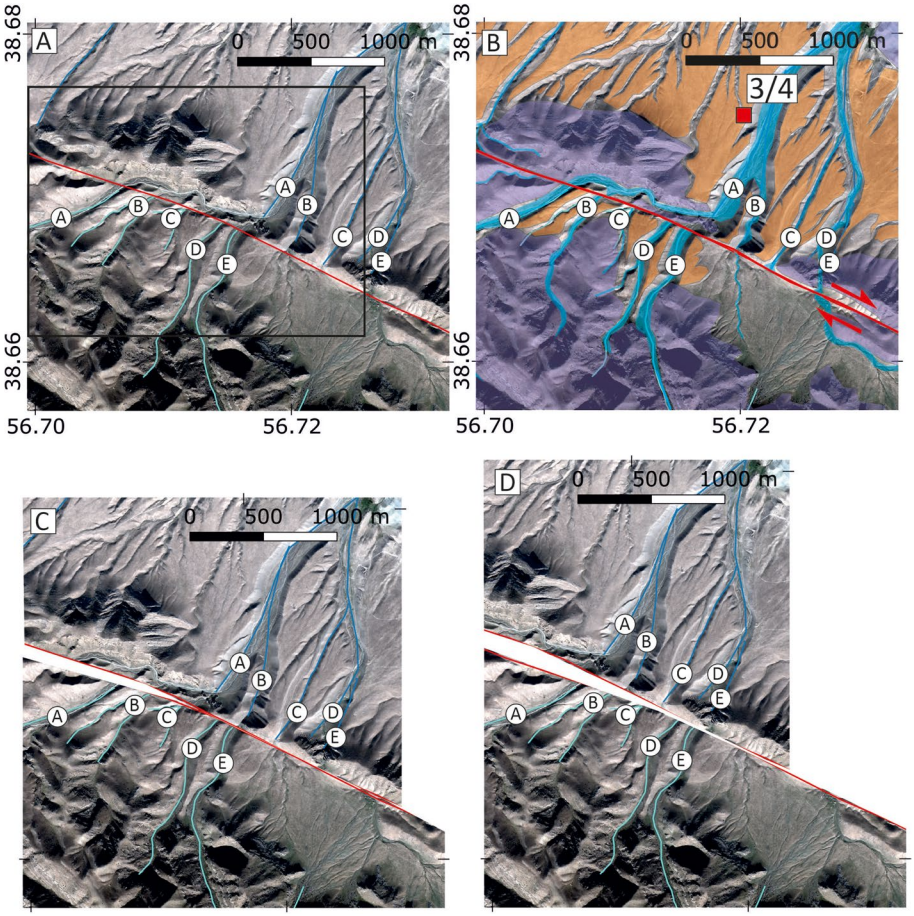

Figure 6. Strike-slip site interpretation and restoration. (a) Worldview-2 satellite image, courtesy of the Digital Globe Foundation, of the sampling site on the strike-slip fault (see Figure 2b for location). The five drainage channels involved in the restoration are labeled A-E. Black box represents the region shown in Figure 7a. (b) Geomorphic map of the site, with the fault shown in red, major drainage in blue, and a well-preserved series of alluvial fan surfaces shown in orange. These alluvial fan deposits are exposed on both sides of the fault. Sample pits 3 and 4 are located within the red square. (c) Restoration of 250–350 m. (d) Restoration of 950 m.

Rivers A-E on the southwest side of the fault all drain into river A on the northeast side. The remaining outlets on the northeast side receive catchment from minor streams or, in the case of D, do not have any catchment. In restoring the right-lateral displacement we assume that the rivers were established as linear courses and have subsequently accrued right-lateral displacement. As there are five closely spaced rivers, restoration of various amounts of slip are successful in aligning several of the channels, suggesting that continued fault slip has led to multiple periods of drainage capture. For instance, 250–350 m of displacement provides a plausible restoration of rivers D and E southwest of the fault with A and B in the northeast (Figure 6c). We acknowledge that the right-lateral offsets of the other rivers may have been influenced by the presence of bedrock outcrops northeast of the fault, such that the rivers may have originally formed with apparent right-lateral deflections around these obstacles. However, as we also find a consistent ~950 m offset that restores all of the rivers A–E to linear courses (Figure 6d), we consider this restoration to be the most parsimonious solution.

We measure the preferred offset of each river using the method shown for river A in Figure 7 (e.g., Kurtz et al., 2018). We trace the channel thalwegs, in blue, and the edges of the valley incision, as shown by yellow highlighting in Figure 7a. The valley edges are projected to the fault (yellow dotted lines). The preferred offset is measured through restoration of the channel thalweg. Any amount of restoration that allows overlap of the yellow polygons is considered plausible, and used to assign an uncertainty range. The values for each of the five rivers are then input as a triangular probability density function (PDF), as shown in Figure 7b,

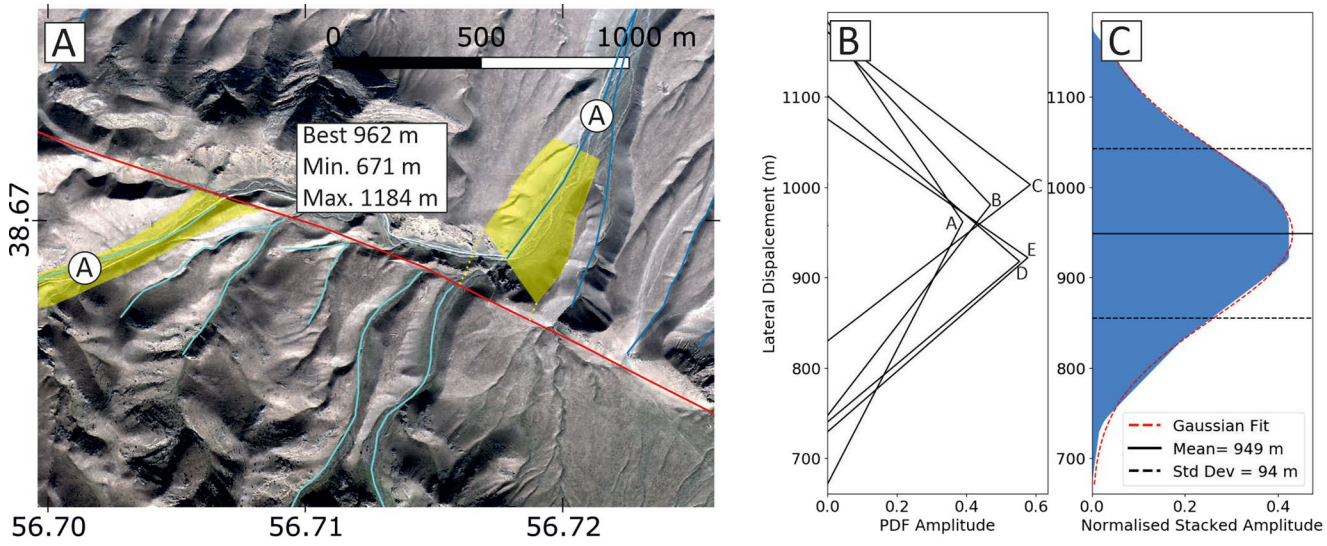

Figure 7. Calculation of offset measurements. (a) Example of offset calculation for channel A. The channel thalweg is marked in blue and the entire channel width in yellow. Preferred offset is assigned from restoration of the thalweg itself, with the range of possible offsets defined as those that allow some overlap of the yellow regions. (b) Probability density functions (PDFs) representing maximum, minimum and preferred measurements of offset for each of the channels A-E. (c) Cumulative offset probability density function (COPD). An assumption is made that the average offset follows a Gaussian distribution, such that the average offset and uncertainty are calculated from the mean and standard deviation of a best-fitting Gaussian distribution [e.g., Kurtz et al., 2018].

and then stacked to form a cumulative offset probability density function (COPD), as shown in Figure 7c. An assumption is made that the average offset follows a Gaussian distribution, such that the average offset and uncertainty are calculated from the mean and standard deviation of a best-fitting Gaussian distribution. The mean offset is 949 m, with uncertainty of ±94 m.

The rivers A to E are incised into an extensive alluvial fan surface (e.g., Figure 5) and we assume that ages of the uppermost fan deposition will approximate to the start of accumulation of displacement by the rivers. We excavated pits into the fan surfaces at four sites (pits 1–4, e.g., Figures 5, 6b and 8). One sample for IRSL (Infra-red-stimulated luminescence) dating was taken from each of pits 1 (38.67743 N 56.69678 E—sample T16-01, taken from the base of a silt layer overlying gravel deposits) and pit 3 (38.67356 N 56.71909 E—sample T16-07, taken from a mixed sand/fine gravel layer within the alluvial sequence). Two samples were taken from pit 4 (38.67529 N 56.72086 E—samples T16-05 and T16-06, both extracted from a sandy silt layer within the alluvial gravel sequence). In pit 2 (38.68587 N 56.67277 E) we encountered hard, cemented, limestone cobbles under a thin (30 cm) soil that was not suitable for sampling for luminescence dating. We instead collected three examples of the pedogenic carbonate cements on the underside of limestone cobbles, from which we drilled individual carbonate layers (Figure B1 in Appendix B) that were dated using the U-series method as described in Gregory et al. (2014) and Campbell et al. (2019). The U-series results are tabulated in Appendix B (Table B1). They yielded ages that were widely variable between the three pebbles, and between sub-samples from the same pebble, and are not considered to be useful.

The IRSL dating results are provided in full in Appendix B (Table B2). We first applied the finite mixture model (FMM) of Galbraith and Green (1990) to identify grouping within the equivalent dose distributions.

Figure 8. Field photograph looking east at Sample pit 3 (Figure 6b) and the incised alluvial fan surface that is right-laterally displaced by ~950 m.

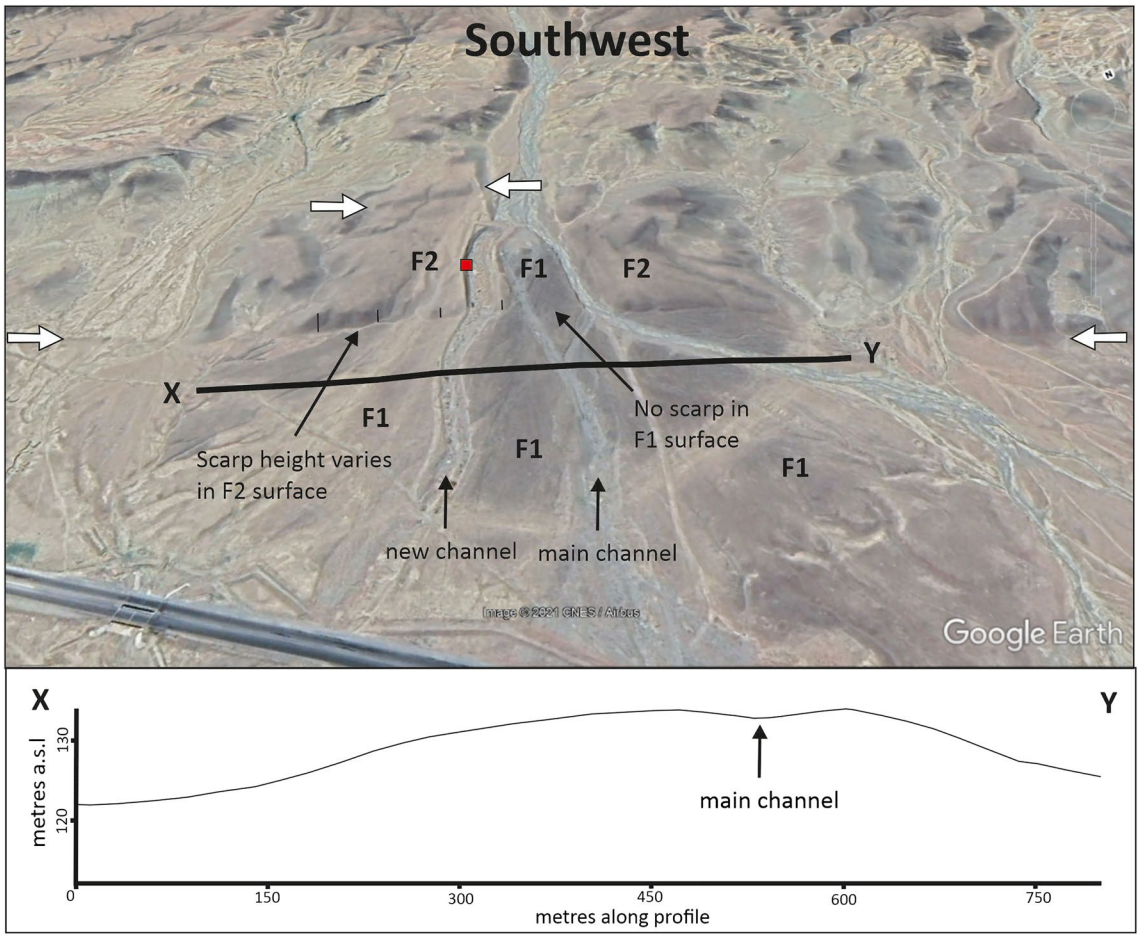

Figure 9. Perspective view looking southwest of the sample site along the reverse fault scarp at Borme (see Figure 2b for location). Topographic profile X-Y is drawn across the convex-up surface of an alluvial fan F1. The surface of fan F1 has been incised by the presently active river channel. Fan F1 is incised into an older alluvial fan F2, which is preserved as remnants on both eastern and western sides of the river catchment. Two fault scarps are visible, and run between the white arrows. The northern of the two faults separates badland topography in its hanging-wall (in distance) from its low-relief footwall (in foreground). The northern (closer) scarp in the F2 surface decreases in height toward the river channel, showing that it has been partially buried by deposition associated with F1. The southern scarp appears to be smaller than the northern one. No scarp is visible in the F1 surface. The red square represents the river-cutting sample location.

We consider all four samples to be contemporaneous based upon the geomorphic setting, as described earlier, and all showed grouping equivalent to ~100 ka in age. We combined the four individual IRSL sample yield ages of 104 ± 8 ka (T16-01), 107 ± 8 ka (T16-05), 91 ± 9 ka (T16-06), and 117 ± 10 ka (T16-07) (Table B2; Figure 6b) using a central age to provide an age estimate of 105,200 ± 4,700 years (see Appendix B). Given a displacement of 949 ± 94 m of the fan surface, this age range yields a slip-rate of 7.8–10.4 mm/yr (or 9.1 ± 1.3 mm/yr).

3.2. Rate of Shortening on the Reverse Fault at Borme

To estimate the rate of shortening across the thrust fault that runs parallel to the main strike-slip fault we collected two IRSL samples (samples T16-03 and T16-04) from a natural river cutting at 38.64065 N 56.89874 E, close to the village of Borme (see Figure 2b). A perspective view looking southwest toward the site is shown in Figure 9 and Worldview-2 satellite imagery and interpretation is shown in Figure 10. A discrete fault scarp displaces the surface of an alluvial fan (F2). The fan surface on the hanging-wall side of the fault has subsequently been incised by a stream, which correlates with a small alluvial fan (F1) in the immediate footwall. The topographic profile along line X-Y in Figure 9 shows the convex-up shape of this

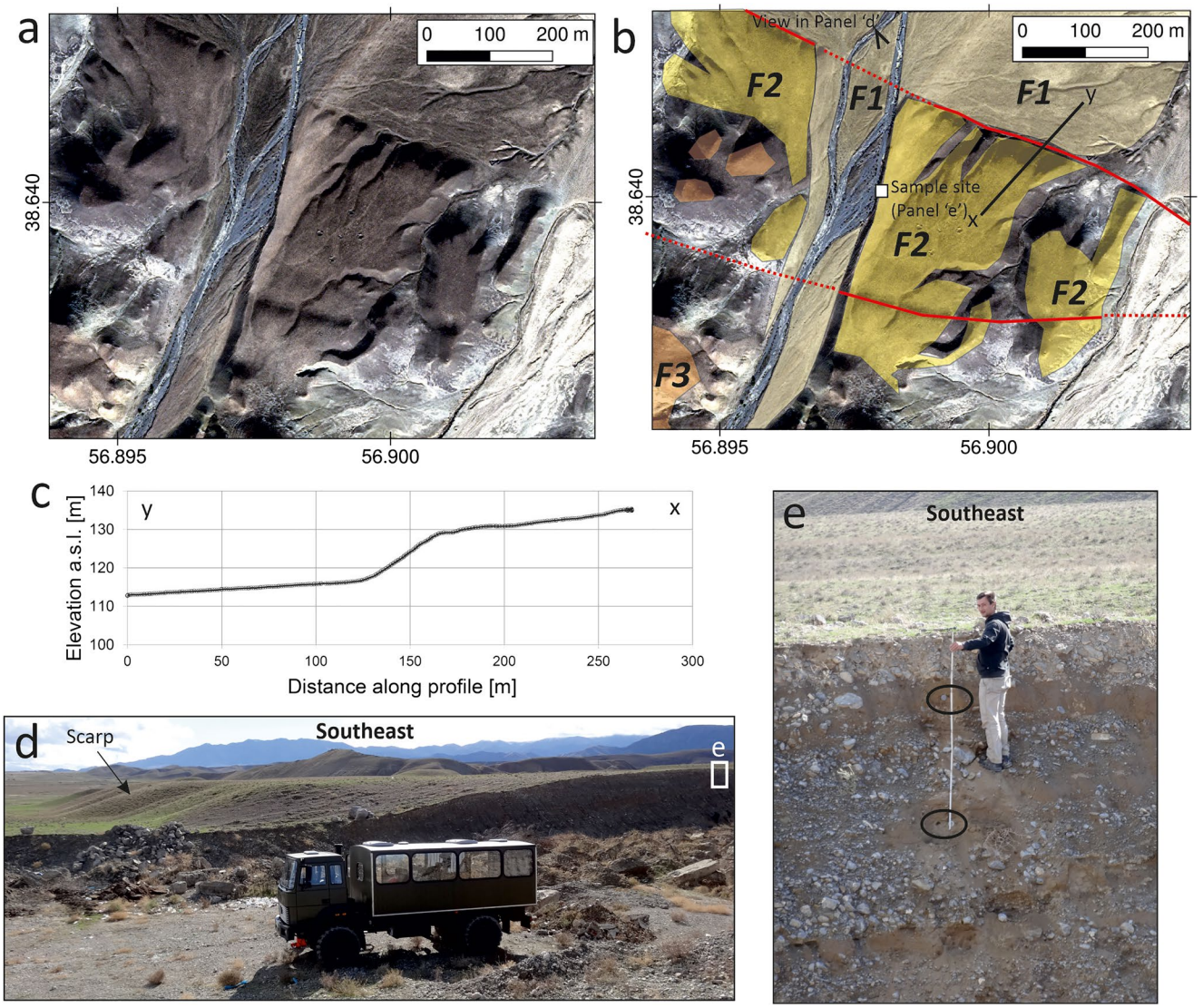

Figure 10. (a) Worldview-2 satellite image, courtesy of the Digital Globe Foundation, of the sampling site on the thrust (see Figure 2b for location). (b) Geomorphic map of the site, with faults shown in red, major drainage in blue, and three generations of alluvial fan surfaces labeled F1 to F3 (youngest to oldest). IRSL sample location is shown. (c) Topographic profile across the frontal thrust, following the black line in "b." (d) Field photograph looking southeast along the frontal scarp from the main river channel. (e) Sample site in the incised river channel margin. Samples taken from sandy silt layers, within the black ellipses.

small fan. F1 is not displaced across the fault, and so post-dates the most recent measureable displacement at the surface.

We used differential kinematic GPS to measure several high-resolution topographic profiles orthogonal to the fault scarp in F2. The scarp height increases with distance away from the stream outlet due to deposition of the young alluvial fan F1 in the immediate footwall of the fault, as evident on Figure 9. The largest vertical displacement that we measured was 12 m on a profile ~200 m from the stream outlet (Figures 10b and 10c). We consider this measurement to be most representative of the displacement since abandonment of the F2 alluvial fan surface but is a minimum value, as we neglect any deposition of younger alluvium in the footwall. A second small scarp is visible in the surface of F2 in the perspective view and Worldview-2 imagery (Figures 9 and 10b), but was not crossed by our GPS profile. We do not have a direct measurement of the height of this second scarp, though from the shadowing visible in the satellite image it appears that it is substantially lower than the frontal scarp. We do not account for the displacement of the F2 surface

across this small scarp, or for any potential broader-wavelength folding or faulting of the F2 surface within the hanging-wall.

The two IRSL samples from F2 (T16-03 and 04) provide an age of 35,600 ± 1,800 years (see Appendix B for full methods), which in turn yield a minimum uplift rate of ~0.3 mm/yr. We do not have a direct estimate of the fault dip to turn this rate into either a rate of shortening or a slip-rate along the fault plane, but assuming a dip of 30–60°S yields a rate of shortening at the surface of 0.2–0.5 mm/yr, and slip along the fault plane of 0.4–0.6 mm/yr. If we further assume that the thrust flattens into a décollement at a relatively shallow depth the overall rate of shortening is likely to be equivalent to the surface fault slip-rate, which will be larger than the 0.3 mm/yr of uplift that we have measured, and possibly in the range 0.4–0.6 mm/yr it the surface dip is in the range 30–60°. We also do not have a constraint on shortening within the hanging-wall of the frontal thrust, which contains additional fault and fold scarps (Figure 2b), and which would add to the overall shortening. The uplift rate of 0.3 mm/yr that we estimate across the frontal thrust is hence a firm minimum value for the overall shortening.

4. Discussion

We determine that the right-lateral slip-rate of the MKDF is 9.1 ± 1.3 mm/yr. This is accompanied by fault orthogonal shortening of at least 0.3 mm/yr, as measured across the frontal thrust. These slip-rates confirm the MKDF to have one of the most rapid known slip-rates of all active faults across the Arabia-Eurasia collision zone, equivalent or larger than the Tabriz fault of NW Iran (Rizza et al., 2013), and comparable to the slip rate on many of the other major strike-slip faults of Asia (e.g., Yeats, 2012). The strike-slip rate of 9.1 ± 1.3 mm/yr is within the wide range of 8.5 ± 3.5 mm/yr permitted from available InSAR measurements of strain accumulation (Walters et al., 2013). In this discussion, we assess the impact of this rate on earthquake hazard, the relative motion of the South Caspian Basin, and the timing of initiation of the presently active structures.

4.1. Earthquake Hazard

Although seismically quiet through recent decades, the potential for devastating earthquakes in Turkmenistan is shown by a magnitude 7.3 event in 1948 that caused widespread damage in the capital city of Aşgabat (e.g.,Berberian & Yeats, 2001; Tchalenko, 1975, Figure 2a), with a present population of ~1 million. The epicenter and strongest shaking from the 1948 earthquake were southeast of the city, and it is likely that it was associated with fault-related folds that are present along the Köpetdag margin adjacent to the city (e.g., Berberian & Yeats, 2001). The region west of Aşgabat was shaken by the M_s 7.0 1929 Bäherden (Baharden) earthquake, which ruptured a N-S right-lateral strike-slip fault of the Quchan-Baharden fault zone (e.g., Hollingsworth et al., 2006; Tchalenko, 1975, Figure 2a). Further west, a number of significant earthquakes have occurred in the Caspian lowlands, including substantial earthquakes of magnitude 6.0–7.5 in 1895, 1946, and 2000, as well as smaller, surface-rupturing, strike-slip earthquakes at Gumdag in 1983 and 1984 (Ambraseys, 1997; Jackson et al., 2002) (Figures 2a and 3). There are few indications of earthquakes in Turkmenistan further back in history, with the only available evidence from archeological investigations. The Parthian city of Nissa, on the western outskirts of the modern city of Aşgabat, shows apparent earthquake-related damage dated to 280 BCE, and earthquake damage at ~2000 BCE is inferred from excavations at the Bronze Age settlement of Ak-Depe, also in the vicinity of Aşgabat (Berberian & Yeats, 2001).

The right-lateral strike-slip MKDF between longitudes 55°E and 57.5°E is a notable gap in the record of recent and historical significant earthquakes (e.g., Figures 2a and 3). Given its length of over two hundred kilometres, the MKDF is potentially capable of producing large ($M_w > 7.5$) earthquakes and measurement of its slip rate is an important step in understanding its earthquake potential. We have shown that slip is accumulating rapidly, at 9.1 ± 1.3 mm/yr. The absence of known historical rupture of the MKDF may indicate that the historical record is incomplete, but it is also likely that significant amounts of slip have accumulated since the most recent event. Paleoseismic investigation of the fault zone is required to discriminate between these possibilities and to build a record of earthquake timing and recurrence.

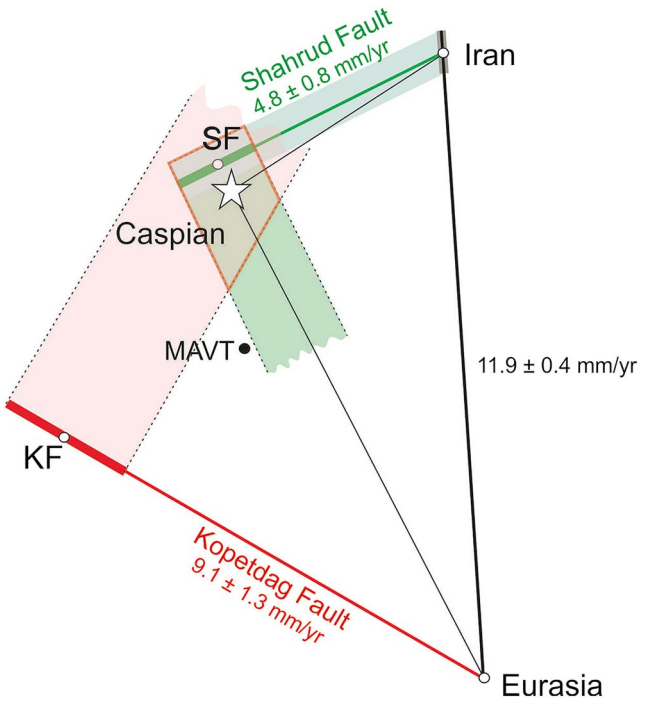

Figure 11. Velocity triangle for calculating the component of shortening associated with motion of the South Caspian Basin (SCB) relative to both Iran and Eurasia, and the motion of the SCB relative to its surroundings. The Iran-Eurasia motion is known from Khorrami et al. (2019) and is 11.9 ± 0.4 mm/yr. The strike-slip component on the Shahrud Fault (SF) is 4.8 ± 0.8 mm/yr toward 244° (Mousavi et al., 2015), which is the green line (with thick error bar) extending WSW from the Iran vertex, with the shaded band allowing for the uncertainty in Iran-Eurasia motion. The strike-slip component on the Kopet Dag Fault (KF) is 9.1 ± 1.3 mm/yr (this paper) toward 300°, which is the red line (with thick error bar) extending NW from the Eurasia vertex. The eastern Alborz and western Köpetdag also accommodate range-perpendicular shortening associated with SCB-Iran and SCB-Eurasia motion, respectively, so the Caspian vertex must lie SSE of SF in the green shaded area and NE of KF in the pink shaded area. The overlap is the quadrilateral outlined in red, with its center point marked by a star. We also mark the velocity of GPS station MAVT.

4.2. Regional Tectonics

We combine our measurement the right-lateral strike-slip rate on the MKDF with constraints on the left-lateral slip-rate on the SFZ in the eastern Alborz, and of the rates of shortening between central Iran (i.e., the low-lying and relatively slowly deforming desert interior) and Eurasia obtained from permanent GPS measurements, to place constraints on the regional tectonic motions through construction of a velocity triangle (Figure 11).

For the Iran-Eurasia motion we use the range in velocity between permanent GPS stations KHUR and MOBK in central Iran (Khorrami et al., 2019, Figure 1), which is 11.5–12.3 mm/yr. The directions of stations KHUR and MOBK are similar, with an average of 358.5°. We select these two stations because they are sited at the longitudes of the eastern South Caspian Basin, such that their velocities are likely to be representative of Central Iran at the longitudes represented in our velocity triangle. They are located within the low-lying and aseismic central Iranian desert, west of the deforming zones of eastern Iran and south of the deformation associated with the Alborz of northern Iran. The uncertainties associated with these permanent stations are also small in comparison to nearby campaign stations (Figure 1).

We separate the relative motion of Iran and the South Caspian into strike-slip parallel to the eastern Alborz and a component of shortening perpendicular to the range. For the range-parallel strike-slip component we use the 4.8 ± 0.8 mm/yr obtained by Mousavi et al. (2015) with InSAR, and a strike of 244°. The Shahrud Fault system (SF) is the main fault identified in the geomorphology and has comparable late Quaternary estimates of slip rate, such that we assume the strain accumulation is likely to be accommodated across this fault, as represented on Figure 11 by the green line (with thick error bar) extending WSW from the Iran vertex, with the gray shaded band allowing for the uncertainty in Iran-Eurasia motion. There is also an unknown amount of shortening in the perpendicular direction, so the Caspian vertex must lie SSE of SF in the green shaded area outlined in dashes. There is no requirement for the shortening to be localized on the Shahrud fault, and it is likely that it is distributed within and at the margins of the eastern Alborz, and also within the lowlands of the eastern Caspian.

We separate the relative motion of the South Caspian and Eurasia into strike-slip parallel to the Köpetdag along with a component of shortening in the perpendicular direction. The Main Köpetdag fault is the only strike-slip fault parallel to the range, and we therefore assume that its slip-rate is representative of the strike-slip component of the South Caspian-Eurasia relative motion. From the measurements presented in this paper, the strike-slip rate on the Main Köpetdag Fault (KF) is 9.1 ± 1.3 mm/yr (this paper) in direction 300°, which is the red line (with thick error bar) extending NW from the Eurasia vertex. Shortening in the perpendicular direction, resulting both from reverse faulting north of the MKDF as well as distributed shortening further south toward the Caspian lowlands, means that the Caspian vertex must lie NE of KF in the pink shaded area outlined in dashes.

The overlap region, consistent with the strike-slip motions on both the Shahroud and Main Köpetdag Faults, and incorporating the expected shortening related to both Iran-South Caspian and Eurasia-South Caspian motion, is the quadrilateral outlined in red. The star in the center is a plausible velocity for the South Caspian Basin and is 10.4 ± 1.1 mm/yr in direction 333° ± 5 relative to Eurasia and at 4.8 ± 0.8 mm/yr in direction 236° ± 14 relative to Iran. These rates compare favorably with earlier estimates of SCB-Eurasia motion of 11 ± 2 mm/yr in direction 335° ± 5 and SCB-Iran motion of 7 ± 1 mm/yr in direction 225°

made by Copley and Jackson (2006). The shortening rate between Eurasia and the SCB, perpendicular to the Köpetdag, is 5.5 ± 1.1 mm/yr and between Iran and the SCB, perpendicular to the eastern Alborz, is 1.0 ± 1.0 mm/yr. Also shown on Figure 11 is the motion of GPS station MAVT in the flat Caspian lowlands of Iran, north of the eastern Alborz (7.7 mm/yr in direction 324° relative to Eurasia). The motion of MAVT is a fair approximation to the motion of the South Caspian Basin, though misses some of the deformation occurring on and between the eastern Alborz and Köpetdag.

4.3. Timing of Initiation of Faulting

The initiation of the presently active tectonics of the SCB is debated. Acceleration in sediment accumulation at 5.5 Ma is often thought to mark increased tectonic subsidence associated with the onset of subduction at that time, though the accelerated sedimentation could also be due to changes in sediment supply and loading, and hence independent of changes in local tectonics (Allen et al., 2003; Green et al., 2009). Devlin et al. (1999) suggest a change in the tectonics of the SCB at ~3.4 Ma from the onset of folding of strata. Paleomagnetic data (Cifelli et al., 2015; Mattei et al., 2017, 2019) indicate that the eastern Alborz and Kopeh Dagh experienced short-lived vertical axis rotation between 4-6 Ma, which the authors interpret as predating the present-day tectonics, followed by an onset of large-scale strike-slip faulting along the Köpetdag from as little as ~2 Ma. Ritz et al. (2006) also argue that the present configuration started as little as 2 Ma, on the basis of a transition from transpressional to transtensional components in the active faults of the Alborz at this time.

The total cumulative right-lateral motion across the MKDF has been estimated at about 35 km (Lyberis & Manby, 1999; Hollingsworth et al., 2006, 2008). The geological displacement of Hollingsworth et al. (2008) comes from the apparent displacement of an anticline exposing folded Neogene to Cretaceous rocks, sited close to Baharly (Figure 2a). They stress that the 35 km is an upper limit for strike-slip displacement, given that they neglect any apparent strike-slip displacement introduced by oblique slip on the fault, though this amount of right-lateral slip is supported by the ~30 km of range-parallel extension in the central Köpetdag estimated by Hollingsworth et al. (2006). Lyberis and Manby (1999) independently estimate ~35 km of right-lateral displacement across the MKDF, but in their case, the estimate comes from resolving 75 km of N-S shortening across the western Köpetdag into orthogonal strike-slip and shortening components.

Hollingsworth et al. (2008) infer the onset of SCB expulsion at ~10 Ma based on an assumed slip rate for the MKDF and the ~35 km of geological displacement as described above. At the faster slip-rate we have estimated here the 35 km of displacement would accumulate in only 3–5 Ma. If the strike-slip offset is less than 35 km then the fault may have initiated more recently. These age estimates are, of course, only approximate. They rely on limited geological data and on an assumption that present-day slip-rates can be extrapolated over millions of years but, nonetheless, appear to support a relatively young timing for the tectonic reorganization of NE Iran and the South Caspian and onset for the present tectonic configuration.

In Section 4.2, we calculated the amounts of shortening expected across the western Köpetdag and eastern Alborz as well as the velocity of the SCB relative to Iran and Eurasia. We use these velocities to estimate the total amounts of strike-slip and shortening expected if the presently active structures initiated at 3–5 Ma. These estimates are, of course, only approximate. They rely on estimates of geological offset on the MKDF that are uncertain, as described above, and an assumption that the slip-rate averaged over ~100 ka is applicable over timescales of millions of years. Nonetheless, the exercise is useful in assessing the possible sense of motion along the Apsheron sill in the central Caspian.

We estimate that shortening between the SCB and Eurasia will occur at 5.5 ± 1.1 mm/yr, resulting in between 13.2 and 33 km of shortening perpendicular to the western Köpetdag at that rate. Shortening between Iran and the SCB in the range 0–2 mm/yr will allow up to 10 km of shortening to accumulate during the most recent tectonic phase. Over the last 3–5 Ma the SCB will have moved by 28–57 km in direction 333° ± 5 relative to Eurasia. Resolving the 333° direction of SCB-Eurasia motion onto the ~295° trend of the Apsheron Sill along the northern margin of the SCB results in ~17–35 km of shortening orthogonal to the sill, and 22–45 km of right-lateral strike-slip parallel to it. Although these estimates are only approximations, they suggest that faulting associated with the Apsheron Sill may have a significant strike-slip component in addition to shortening, and that the total amount of shortening within the present tectonic regime may be

relatively modest. Our results do not, however, resolve whether the subduction of SCB basement initiated with the onset of the present tectonic phase (e.g., Jackson et al., 2002) or whether it began earlier (e.g., Green et al., 2009).

5. Conclusions

With a right-lateral strike-slip rate of 9.1 ± 1.3 mm/yr the Main Köpetdag fault of Turkmenistan is amongst the fastest moving of all faults within the Arabia-Eurasia continental collision. Our result has implications for the hazard posed by the fault, for which there is no historic record of significant earthquakes over much of its length. Our slip-rate estimate, when combined with existing estimates of left-lateral slip-rate on the Shahroud fault of Iran and of Iran-Eurasia shortening, allows us to calculate that the direction and magnitude of motion of the South Caspian Basin relative to its surroundings. Our ability to make this measurement offers a significant advancement in our understanding the tectonic development of this enigmatic, aseismic, and predominantly water-covered block within the wider Arabia-Eurasia continental collision.

Appendix A: Earthquake Source Parameters

Figure 3 contains an update of the earthquakes with reliable teleseismically determined source parameters in the Caspian region, updating the earlier compilation by Jackson et al. (2002). The new earthquakes are listed in Tables A1–A3. Table A1 contains those whose parameters are estimated from long-period P and SH body-wave modeling, using the method and velocity structures described by Jackson et al. (2002). Their waveforms are shown in Figures A1–A5.

Table A1
Earthquakes in Figures 3b and 3d in Addition to Those Listed in Jackson et al. (2002), Whose Centroid Depths Have Been Obtained Through Body-Waveform Modeling, as Described Above

Date			Time				Depth					
Yr	Mo	Day	Hr	Min	Lat.	Long	km	Mw	Strike	Dip	Rake	Reference
1999	11	19	4	40	36.92	54.9	26	5.4	80	32	78	Nemati et al. (2013)
2000	1	26	23	0	40.02	52.9	50	5.1	358	37	174	Figure A1
2004	5	28	12	38	36.29	51.61	22	6.2	110	34	76	Tatar et al. (2007)
2004	10	7	21	46	37.13	54.48	28	5.5	47	44	71	Nemati et al. (2013)
2005	1	10	18	47	37.1	54.57	29	5.2	69	31	68	Nemati et al. (2013)
2006	10	12	17	8	39.76	54.7	41	5.1	111	70	119	Figure A2
2014	2	10	2	6	40.29	48.8	59	5.3	219	40	−179	Figure A3
2016	10	26	14	15	39.49	54.41	28	5.3	311	30	124	Figure A4
2017	5	13	18	1	37.77	57.2	5	5.6	182	79	−172	Figure A5

Table A2
Earthquakes in Figure 3b in Addition to Those Listed in Jackson et al. (2002), Whose Source Parameters are Taken From the gCMT Catalog

Date			Time				Depth					
Yr	Mo	Day	Hr	Min	Lat.	Long	km	Mw	Strike	Dip	Rake	%dc
2012	1	19	12	35	36.29	58.83	19	5.3	292	24	80	82
Additional small earthquakes from the eastern Caspian lowlands												
2000	9	19	15	19	38.3	57.48	32	5.1	40	78	−3	91
2002	10	19	15	57	39.04	54.91	18	5.1	214	52	39	85

Table A2
Continued

Date			Time				Depth					
Yr	Mo	Day	Hr	Min	Lat.	Long	km	Mw	Strike	Dip	Rake	%dc
2012	10	1	8	43	38.5	55.54	17	4.9	217	70	7	96
2013	12	9	1,133		38.6	55.6	12	5.1	209	73	16	97
2014	2	13	8	35	38.59	56.24	21	5	313	89	−179	79
2017	2	5	13	46	39.26	54.81	13	4.9	47	32	67	86
2017	2	5	15	59	39.3	54.73	14	4.8	81	26	114	99

Note. For consistency with Jackson et al. (2002), only those with centroids shallower than 34 km, with Mw ≥ 5.3 and with more than 70% double-couple solutions should be included (line 1 only). But smaller earthquakes from the eastern Caspian lowlands have been included (lines 3–9), to show all that are available.

Table A3
Earthquakes in Figure 3d in Addition to Those Listed in Jackson et al. (2002), Whose Source Parameters are Taken From the gCMT Catalog

Date			Time				Depth					
Yr	Mo	Day	Hr	Min	Lat.	Long	km	Mw	Strike	Dip	Rake	%dc
2001	6	10	1	52	39.87	53.89	57	5.4	315	35	116	69
2006	10	12	17	8	39.8	54.73	48	5.3	273	26	74	74
2009	6	2	14	39	40.28	53.01	58	5	229	63	−26	92
2012	10	7	11	42	40.75	48.44	44	5.1	284	36	−103	89
2014	1	14	13	55	40.28	52.88	45	5	288	38	81	96
2014	6	7	6	5	40.37	51.57	46	5.4	127	24	−64	57
2015	3	22	22	45	40.27	52.07	39	5.1	170	70	19	83

Note. Only those with centroids deeper than 28 km, with $M_w \geq 5$ and with more than 40% double-couple solutions are selected.

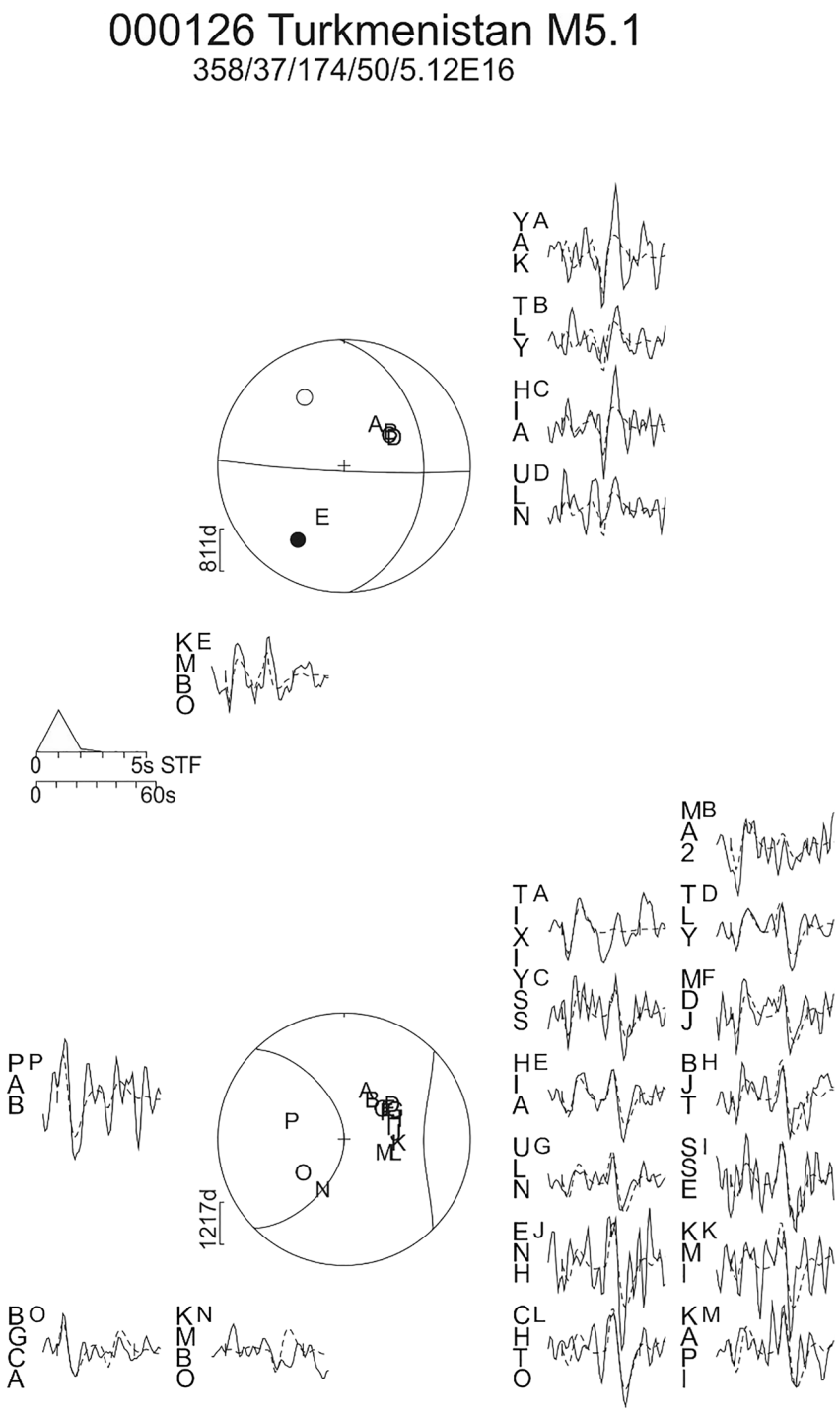

Figure A1. P (top) and SH (bottom) nodal planes and waveforms (observed, solid; synthetic, dashed) for the January 26, 2000 on the Caspian coast of Turkmenistan. Numbers beneath the heading are strike/dip/rake/centroid depth/seismic moment (in Nm). The station code for each waveform is accompanied by a letter identifying its position on the focal sphere, arranged clockwise alphabetically. The time window used for the inversion is marked by vertical bars on each waveform. P and T axes are solid and open circles on the P focal sphere. STF is the Source Time Function. The 50 km depth is well constrained by the clear surface reflection at YAK, HIA and KMO (for P) and eastern stations for SH. The gCMT depth was 65 km.

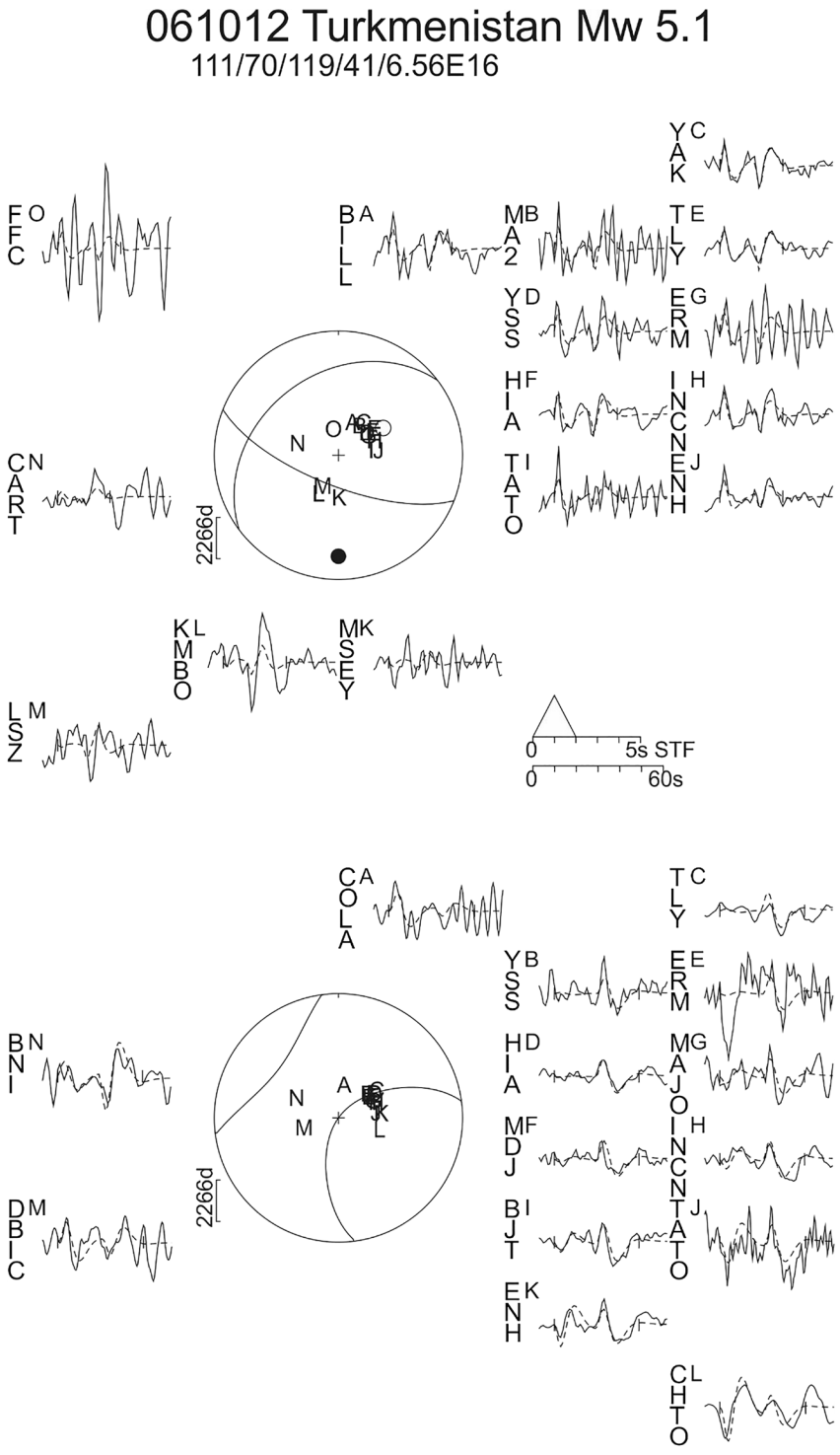

Figure A2. P (top) and SH (bottom) nodal planes and waveforms for the October 12, 2006 earthquake in the Caspian lowlands of Turkmenistan. The depth of 41 km is well constrained by the surface reflections at YAK, TLY, HIA (for P) and HIA, MAGO, BNI for SH. The gCMT depth was 48 km.

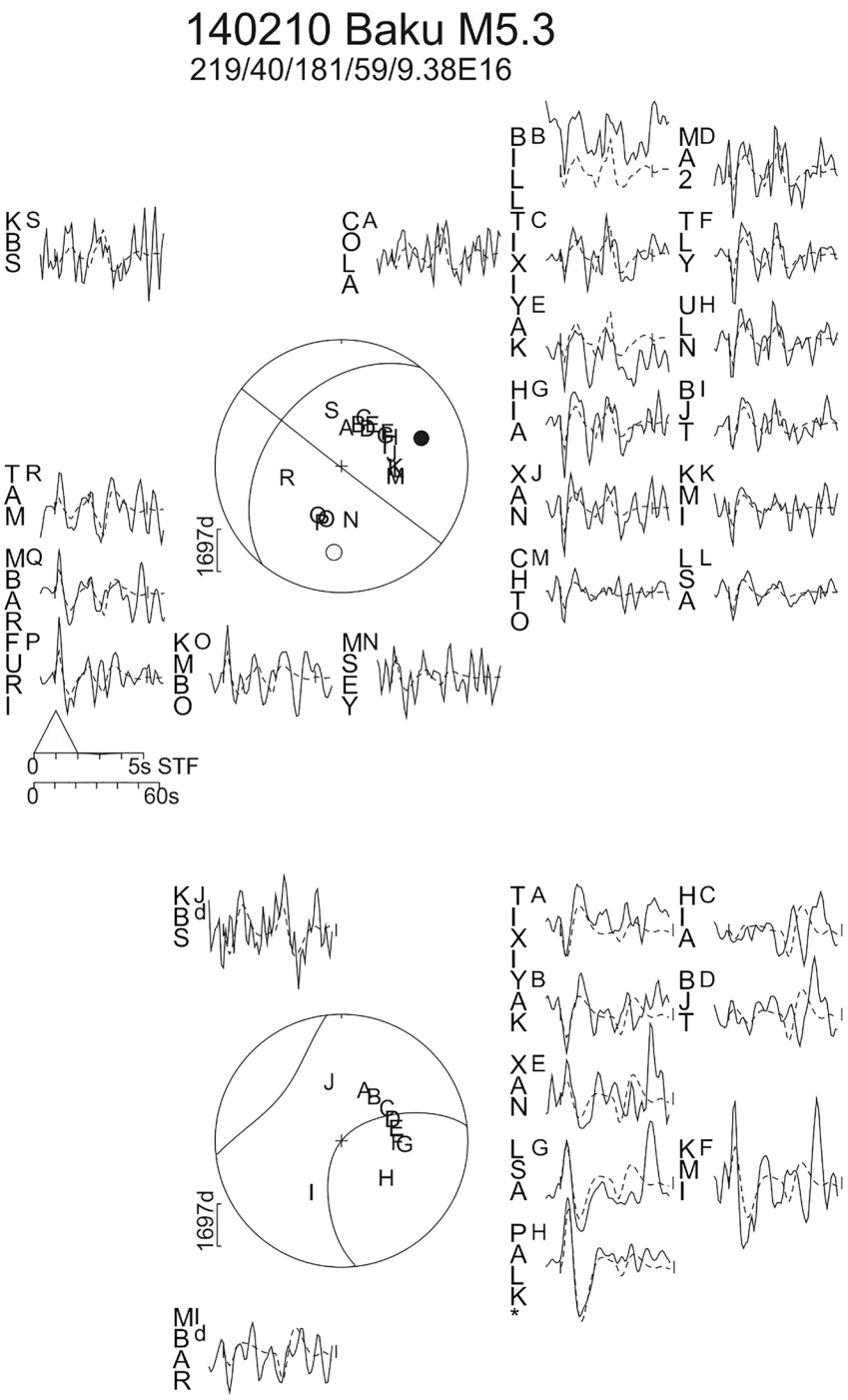

Figure A3. P (top) and SH (bottom) nodal planes and waveforms for the February 10, 2014 earthquake near Baku in Azerbaijan. Seismograms are noisy for this event, but surface reflections at stations in the NE (for P) and KBS (for SH) support the depth of about 59 km (The sS surface reflection lies near a nodal plane for most of the other SH stations). The depth of 41 km is well constrained by the surface reflections at YAK, TLY, HIA (for P) and HIA, MAGO, BNI for SH. The gCMT depth was 69 km.

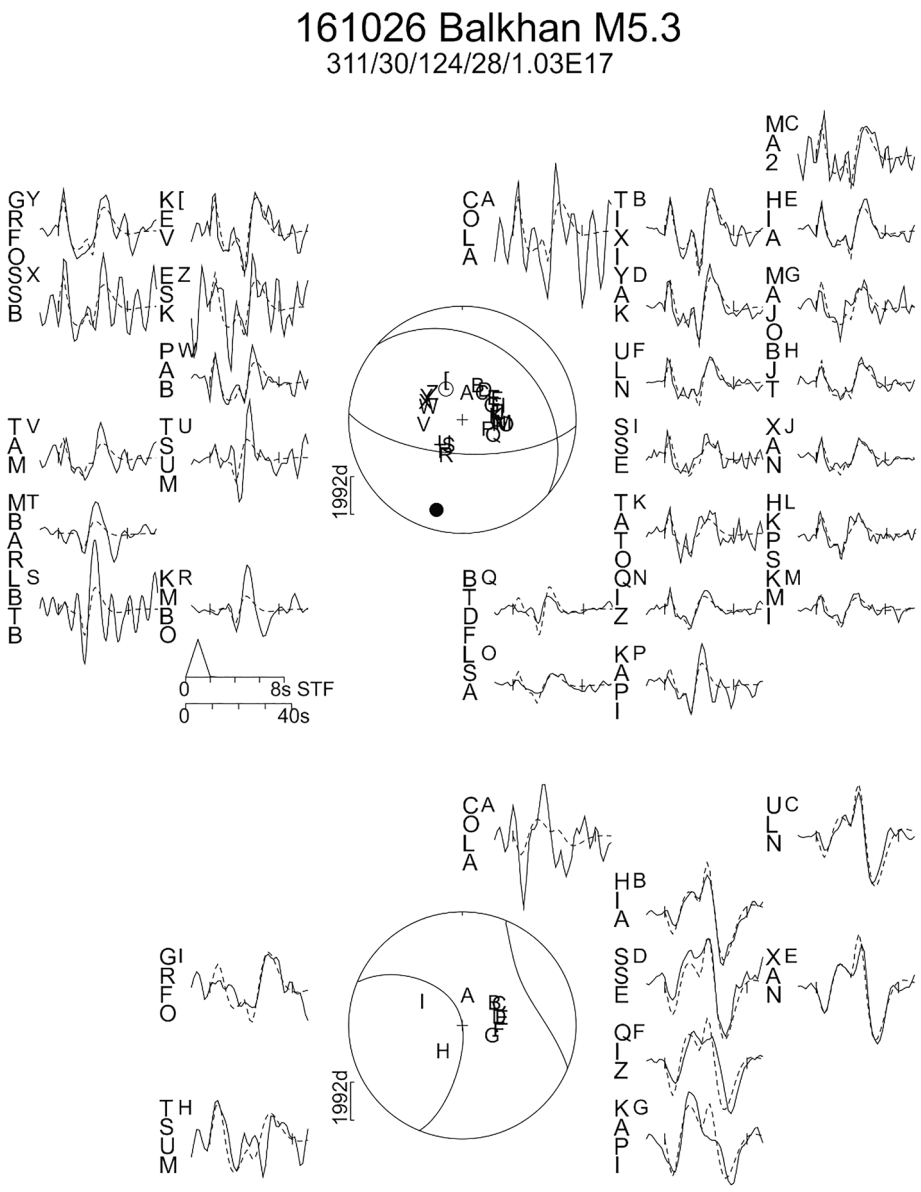

Figure A4. P (top) and SH (bottom) nodal planes and waveforms for the October 26, 2016 earthquake in the Balkhan region of coastal Turkmenistan. The depth of 28 km is well constrained by clear surface reflections at many stations. The gCMT depth was 28 km.

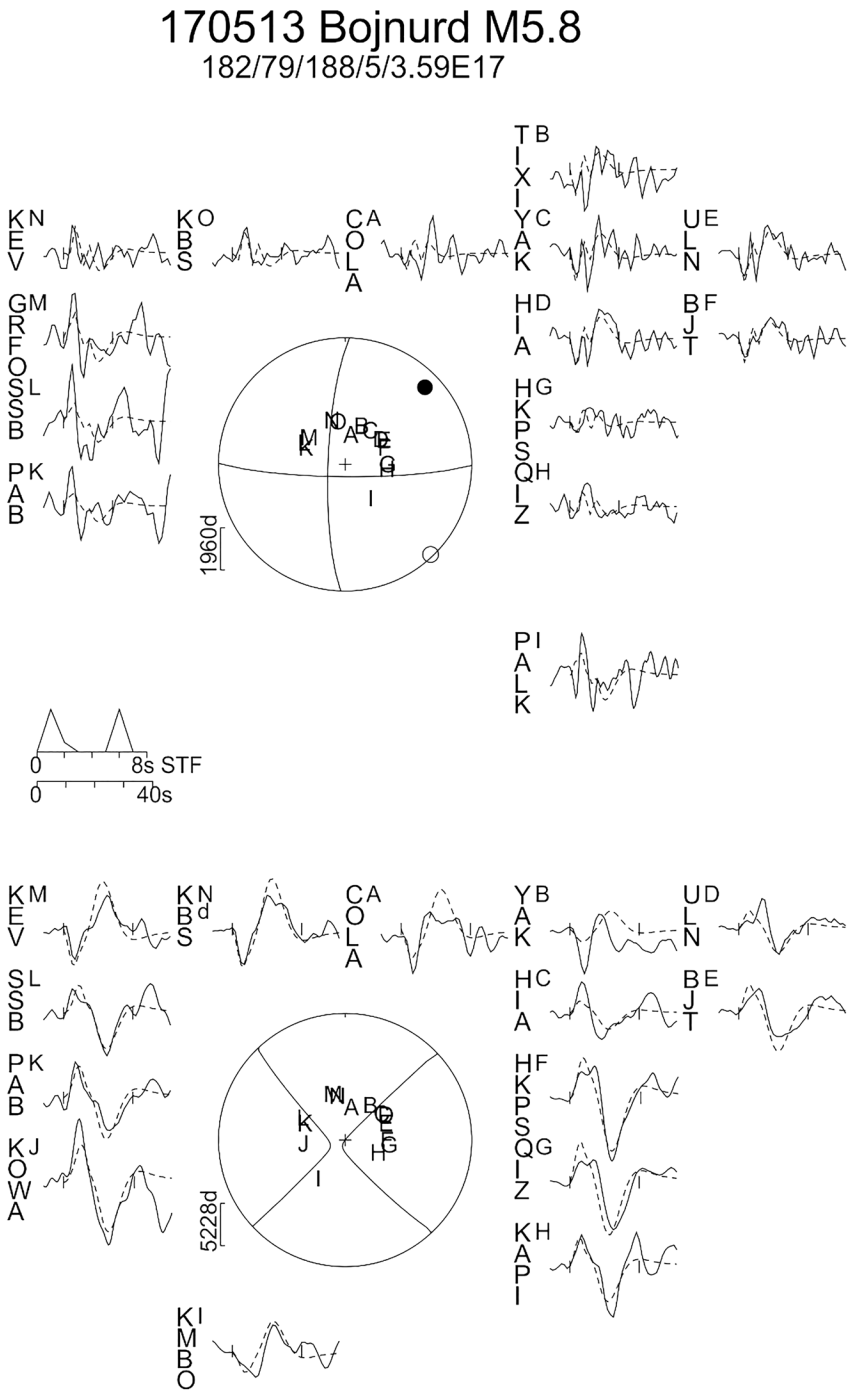

Figure A5. P (top) and SH (bottom) nodal planes and waveforms for the May 13, 2017 earthquake near Bojnurd in the Kopet Dag. The earthquake was a double event, seen in the STF, which is responsible for the double-downward pulse at NE stations (which cannot be due to pP which is up), and the shallow depth is well constrained. The gCMT depth was fixed at 12 km.

Appendix B: Quaternary Dating Methods

In this appendix, we present a full U-series data table (Table B1) and photographs of the sampled carbonate horizons (Figure B1). The U-series methods are as described in Gregory et al. (2014) and Campbell et al. (2019). In Table B2 we present full details of the luminescence dating and in Figure B2 we present the plots of single-grain IRSL measurements for each of the six samples used in this study. The IRSL field sampling is as described in Grutzner et al. (2017). Sample preparation followed standard K-feldspar treatments, incorporating a density separation at 2.58 gcm^{-3} with no etch, applied to 180–212 μm grains.

Table B1
U-Th Ages of Five Calcite Subsamples Drilled From Pedogenic Carbonate Cements on the Underside of Limestone Cobbles (Figure SX)

Sample	^{238}U (ppm)	^{232}Th (ppm)	$(^{234}U/^{238}U)_{act}$ (1 s-rel.)	$(^{230}Th/^{238}U)_{act}$ (1 s-rel.)	$(^{232}Th/^{238}U)_{act}$ (1 s-rel.)	Uncorrected age (years BP)	Corrected age (years BP)	Age error (−2 s; years)	Age error (+2 s; years)	Initial $(^{234}U/^{238}U)_{act}$	% Meas. ^{230}Th from detrital material
T16-02A	1.777	0.470	1.141 (0.2%)	1.016 (0.2%)	0.0866 (0.3%)	217,000	209,000	9,000	9,000	1.254	1.3%
T16-02B	2.832	0.574	1.098 (0.2%)	1.037 (0.2%)	0.0663 (0.3%)	276,000	270,000	9,000	9,000	1.209	0.5%
T16-02C	2.011	0.675	1.164 (0.2%)	1.224 (0.2%)	0.1098 (0.2%)	570,000	560,000	70,000	130,000	1.804	0.1%
T16-02D	1.468	0.355	1.139 (0.2%)	1.102 (0.2%)	0.0790 (0.2%)	294,000	286,000	12,000	12,000	1.311	0.5%
T16-02E	1.214	0.795	1.159 (0.3%)	1.188 (0.3%)	0.2144 (0.3%)	410,000	390,000	40,000	40,000	1.477	0.5%

Note. Measured isotope ratios were analyzed on a Nu Plasma MC-ICP-MS at the University of Oxford. Corrected ages account for initial detrital ^{230}Th present in sample, based on the ^{232}Th concentration in the sample and the average continental crust atomic ratio, $^{230}Th/^{232}Th = 5.4 \pm 5.4$ ppm (uniform distribution). Age error (2 sigma) was calculated using a Monte Carlo simulation. Years BP is years before 1950 CE.

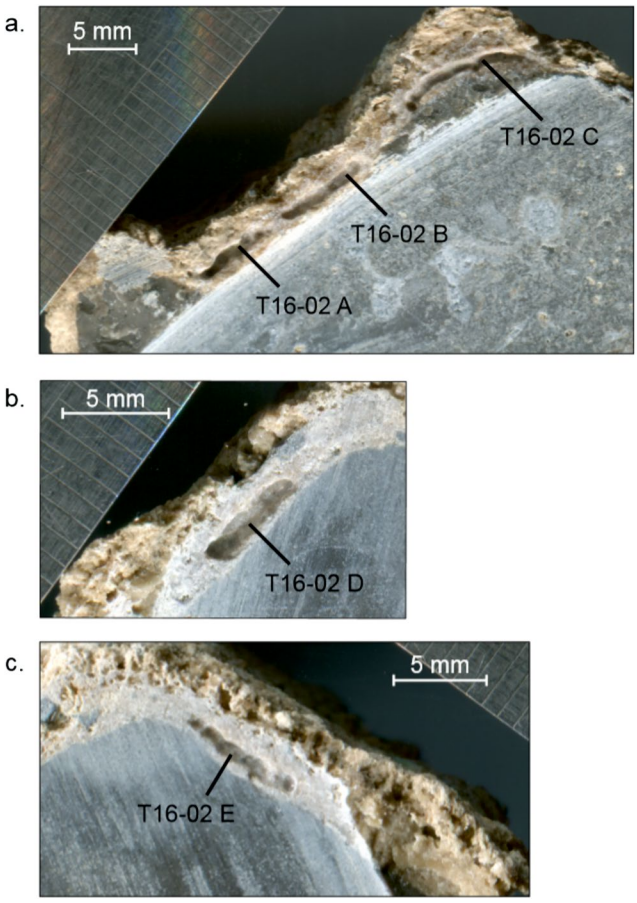

Figure B1. Photographs of the five carbonate layers from three clasts selected for U-series age determination. All three clasts were taken from Sample Pit 2, see main text. The resulting ages are given in Table B1.

Single grain post-infra-red infra-red stimulated luminescence (Post-IR IRSL) measurements on K-Feldspar grains were made in the Sheffield luminescence laboratory using the approach described in Rhodes (2015) and Zinke et al. (2017). Some samples displayed grouped equivalent dose distributions (see figures in appendix), and for these four samples the finite mixture model (FMM) of Galbraith and Green (1990) was used, implemented using the software of Burow (2020) in R. Three of the four samples analyzed using the FMM are from the same surface (see main text), and must therefore have the same depositional age, and the fourth (T16-01) comes from a nearby surface that appears of similar age based upon our geomorphic interpretations, allowing us to treat all for samples as contemporaneous. All displayed a significant age component at around 100,000 years which is considered the most likely depositional age for these samples. The FMM for each IRSL sample yield ages of 104 ± 8 ka (T16-01), 107 ± 8 ka (T16-05), 91 ± 9 ka (T16-06), and 117 ± 10 ka (T16-07) (Table B2; Figure 6b). We combined these four ages using a central age approach

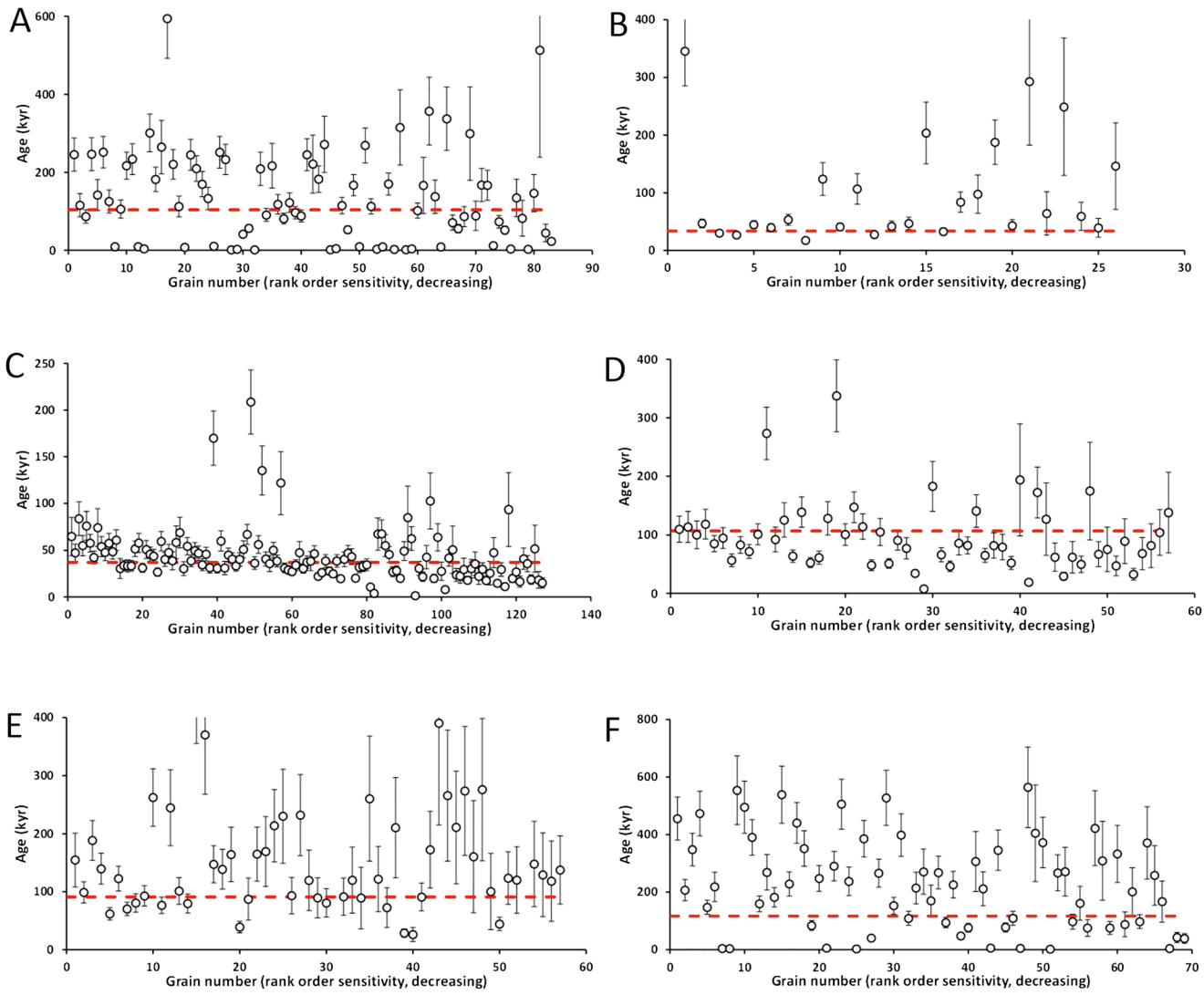

Figure B2. Grain age distributions for each of the six samples. (a) T16-01 Shfd-17051 Measured single grain post-IR $IRSL_{225}$ data; dashed line represents FMM age estimate of 104 ± 8 ka (see Table B1). (b) T16-03 Shfd-17053 Measured single grain post-IR $IRSL_{225}$ data; dashed line represents discrete minimum age estimate of 34 ± 3 ka (see Table B1). (c) T16-04 Shfd-17054 Measured single grain post-IR $IRSL_{225}$ data; dashed line represents discrete minimum age estimate of 37 ± 2 ka (see Table B1). (d) T16-05 Shfd-17055 Measured single grain post-IR $IRSL_{225}$ data; dashed line represents FMM age estimate of 107 ± 8 ka (see Table B1). (e) T16-06 Shfd-17056 Measured single grain post-IR $IRSL_{225}$ data; dashed line represents FMM age estimate of 91 ± 7 ka (see Table B1). (f) T16-07 Shfd-17057 Measured single grain post-IR $IRSL_{225}$ data; dashed line represents FMM age estimate of 117 ± 9 ka (see Table B1).

with zero overdispersion, with systematic uncertainty removed from individual ages, and a systematic uncertainty of 2% added in quadrature to the combined result; for these samples this provides an age estimate of 105,200 ± 4,700 years.

Two remaining samples (T16-03 and 04, Table B2) were analyzed by the discrete minimum approach described in Rhodes (2015). An overdispersion value of 15% was used for all samples, based on previous experience from age-controlled single grain samples from Australian geoarcheological contexts (Rhodes et al., 2010). Every grain measured was assessed for fading; no indication of significant systematic fading was observed. Sediment dose rates were estimated using ICP-OES for K and ICP-MS for U and Th, corrected for water and grain size attenuation, and internal dose rate estimation assumed an internal K content of 12.5 ± 2.5% (Huntley & Baril, 1997). The two individual sample ages were then combined, using a similar approach as described above, to provide an age of 35,600 ± 1,800 years.

Tectonics

10.1029/2021TC006846

Table B2
Field Code, Sample Locations, Laboratory Code, and Depth for Single Grain K-Feldspar Post-IR IRSL at 225°C Sediment Dating Samples

Field code	Notes	Lab code	Depth (m)	Sediment K (%)	Sediment U (μg/g)	Sediment Th (μg/g)	Dose rate mGy/yr	1 sigma uncertainty	Grain numbers measured/signal	Equivalent Dose (Gy)	1 sigma uncertainty	Age (kyr)	1 sigma uncertainty	Proportion
T16-01	Site D, pit, river terrace	Shfd-17051	0.6	1	2.2	6.1	2.64	±0.13	200/83	7.4	±0.5	2.8	±0.2	0.14
										25.9	±1.7	9.8	±0.8	0.1
										135	±12	51	±5	0.08
										274	**±16**	**104**	**±8**	**0.27**
										618	±26	234	±15	0.4
T16-03	Site F, river bank	Shfd-17053	1.80	1.3	3.5	7.6	3.23	±0.13	200/26	108	±8	34	±3	
T16-04	Site F, river bank	Shfd-17054	0.60	1.5	2.4	8.4	3.26	±0.16	200/127	119	±4	37	±2	
T16-05	Nr site D, pit, river terrace	Shfd-17055	1.1	1.3	2.2	7.3	2.95	±0.13	200/57	24.2	±3.9	8.2	±1.4	0.02
										83.6	±9.7	28	±4	0.06
										179	±14	61	±5	0.35
										317	**±19**	**107**	**±8**	**0.53**
										826	±116	280	±41	0.04
T16-06	Nr site D, pit, river terrace	Shfd-17056	1.1	0.9	1.8	4.8	2.37	±0.1	200/57	85.7	±13.9	36	±6	0.07
										215	**±19**	**91**	**±9**	**0.43**
										482	±49	203	±22	0.47
										4,000	±1,332	1,690	±568	0.03
T16-07	Nr site D, pit, river terrace	Shfd-17057	1	0.6	1.7	2.8	1.95	±0.09	200/69	8.8	±0.7	4.5	±0.4	0.12
										87.3	±12.1	45	±7	0.06
										229	**±17**	**117**	**±10**	**0.26**
										674	±29	345	±21	0.57

Note. Also shown are sediment concentrations of K (ICP-OES determination), U and Th (ICP-MS determinations), the total dose rate including internal beta dose rate contribution and cosmic dose rate, adjusted for water and grain size attenuation. The numbers of grains measured and the numbers that provided a finite age estimate are shown. Several samples displayed significant clustering of equivalent dose values, and these were analyzed using a finite mixture model (FMM); results for these are shown in bold type and represent the values most likely to represent depositional age. The final column shows the proportion of results for that sample apportioned by the FMM to each age estimate. See text for further details.

Data Availability Statement

FAIR data access statement: Commercial Worldview-2 data used within this analysis were obtained through application to the DigitalGlobe foundation and are available for purchase from Maxar (https://www.maxar.com/). Stereo SPOT-6 data were purchased under academic licence from Airbus and are available for purchase (https://www.airbus.com/space.html). Seismological analyses use data archived by IRIS (iris.edu/hq/) and the Global CMT catalog (https://www.globalcmt.org/). All data derived from IRSL and U-series dating is provided in full within the main body of the paper, and archived in Zenodo at http://doi.org/10.5281/zenodo.5037978 (Walker et al., 2021). We thank Prof. Siddharth Saxena of the Cambridge Central Asia Forum, Vepa Malikgulyyev, Murad Kakajykov of the UK embassy in Turkmenistan, and the Ambassador of Turkmenistan to the UK for their kind help and logistical support. We thank the President of Turkmenistan for his support of the joint Turkmenistan-UK Scientific collaboration.

Acknowledgments
This work was supported by the Leverhulme Trust Research Project Grants "EROICA" (RPG-2018-371) and "NEPTUNE" (RPG-2018-243), by the NERC-ESRC Increasing Resilience to Natural Hazards program "Earthquakes without Frontiers" (NE/J02001X/1), the NERC-funded COMET (GA/13/M/031), and allocation 0009090 from the Research England GCRF Support Fund. Worldview-2 satellite imagery was courtesy of the DigitalGlobe Foundation. Maps were prepared using Generic Mapping Tools software (Wessel & Smith, 1995). We thank Massimo Mattei, Stefano Tavani, an anonymous reviewer, and Associate Editor Jessica Thompson Jobe for detailed and constructive comments that helped shape the paper.

References

Allen, M. B., Jones, S., Ismail-Zadeh, A., Simmons, M., & Anderson, L. (2002). Onset of subduction as the cause of rapid Pliocene-Quaternary subsidence in the South Caspian basin. *Geology*, *30*(9), 775–778. https://doi.org/10.1130/0091-7613(2002)030<0775:oosatc>2.0.co;2

Allen, M. B., Vincent, S. J., Alsop, G. I., Ismail-zadeh, A., & Flecker, R. (2003). Late Cenozoic deformation in the South Caspian region: Effects of a rigid basement block within a collision zone. *Tectonophysics*, *366*(3–4), 223–239. https://doi.org/10.1016/s0040-1951(03)00098-2

Ambraseys, N. N. (1997). The Krasnovodsk (Turkmenistan) earthquake of 8 July 1895. *Journal of Earthquake Engineering*, *1*(02), 293–317. https://doi.org/10.1080/13632469708962370

Ambraseys, N. N., & Melville, C. P. (2005). *A history of Persian earthquakes*. Cambridge university press.

Aziz Zanjani, A., Ghods, A., Sobouti, F., Bergman, E., Mortezanejad, G., Priestley, K., et al. (2013). Seismicity in the western coast of the South Caspian Basin and the Talesh Mountains. *Geophysical Journal International*, *195*(2), 799–814. https://doi.org/10.1093/gji/ggt299

Berberian, M. (2014). *Earthquakes and coseismic surface faulting on the Iranian Plateau* (Vol. 17). Elsevier.

Berberian, M., & Yeats, R. S. (2001). Contribution of archaeological data to studies of earthquake history in the Iranian Plateau. *Journal of Structural Geology*, *23*(2–3), 563–584. https://doi.org/10.1016/s0191-8141(00)00115-2

Burow, C. (2020). calc_FiniteMixture: Apply the finite mixture model (FMM) after Galbraith (2005) to a given De distribution. Function version 0.4.1. In S. Kreutzer, C. Burow, M. Dietze, M. C. Fuchs, C. Schmidt, M. Fischer, et al. (Eds.), *Luminescence: Comprehensive Luminescence Dating Data Analysis. R package version 0.9.10*. Retrieved from https://CRAN.R-project.org/package=Luminescence

Campbell, G. E., Walker, R. T., Abdrakhmatov, K., Carolin, S., Carr, A. S., Elliott, J. R., et al. (2019). Rapid late quaternary slip, repeated prehistoric earthquake rupture, and widespread landsliding associated with the Karakudzhur Thrust, Central Kyrgyz Tien Shan. *Tectonics*, *38*(11), 3740–3764. https://doi.org/10.1029/2018tc005433

Cifelli, F., Ballato, P., Alimohammadian, H., Sabouri, J., & Mattei, M. (2015). Tectonic magnetic lineation and oroclinal bending of the Alborz range: Implications on the Iran-Southern Caspian geodynamics. *Tectonics*, *34*(1), 116–132. https://doi.org/10.1002/2014tc003626

Copley, A., & Jackson, J. (2006). Active tectonics of the Turkish-Iranian plateau. *Tectonics*, *25*(6). https://doi.org/10.1029/2005tc001906

Cowgill, E., Forte, A. M., Niemi, N., Avdeev, B., Tye, A., Trexler, C., et al. (2016). Relict basin closure and crustal shortening budgets during continental collision: An example from Caucasus sediment provenance. *Tectonics*, *35*(12), 2918–2947. https://doi.org/10.1002/2016tc004295

Devlin, W., Cogswell, J., Gaskins, G., Isaksen, G., Pitcher, D., Puls, D., et al. (1999). South Caspian Basin: Young, cool, and full of promise. *Geological Society of America Today*, *9*(7), 1–9.

Djamour, Y., Vernant, P., Bayer, R., Nankali, H. R., Ritz, J. F., Hinderer, J., et al. (2010). GPS and gravity constraints on continental deformation in the Alborz mountain range, Iran. *Geophysical Journal International*, *183*(3), 1287–1301. https://doi.org/10.1111/j.1365-246x.2010.04811.x

Galbraith, R. F., & Green, P. F. (1990). Estimating the component ages in a finite mixture. *International Journal of Radiation Applications and Instrumentation - Part D: Nuclear Tracks and Radiation Measurements*, *17*(3), 197–206. https://doi.org/10.1016/1359-0189(90)90035-v

Ghassemi, M. R., & Garzanti, E. (2019). Geology and geomorphology of Turkmenistan: A review. *Geopersia*, *9*(1), 125–140.

Grützner, C., Carson, E., Walker, R. T., Rhodes, E. J., Mukambayev, A., Mackenzie, D., et al. (2017). Assessing the activity of faults in continental interiors: Paleoseismic insights from SE Kazakhstan. *Earth and Planetary Science Letters*, *459*, 93–104. https://doi.org/10.1016/j.epsl.2016.11.025

Green, T., Abdullayev, N., Hossack, J., Riley, G., & Roberts, A. M. (2009). Sedimentation and subsidence in the south Caspian Basin, Azerbaijan. *Geological Society, London, Special Publications*, *312*(1), 241–260. https://doi.org/10.1144/sp312.12

Gregory, L. C., Thomas, A. L., Walker, R. T., Garland, R., Mac Niocaill, C., Fenton, C. R., et al. (2014). Combined uranium series and 10Be cosmogenic exposure dating of surface abandonment: A case study from the Ölgiy strike-slip fault in western Mongolia. *Quaternary Geochronology*, *24*, 27–43. https://doi.org/10.1016/j.quageo.2014.07.005

Hollingsworth, J. (2008). *Active tectonics of NE Iran* (PhD Thesis). University of Cambridge.

Hollingsworth, J., Fattahi, M., Walker, R., Talebian, M., Bahroudi, A., Bolourchi, M. J., et al. (2010). Oroclinal bending, distributed thrust and strike-slip faulting, and the accommodation of Arabia–Eurasia convergence in NE Iran since the Oligocene. *Geophysical Journal International*, *181*(3), 1214–1246.

Hollingsworth, J., Jackson, J., Walker, R., & Nazari, H. (2008). Extrusion tectonics and subduction in the eastern South Caspian region since 10 Ma. *Geology*, *36*(10), 763–766. https://doi.org/10.1130/g25008a.1

Hollingsworth, J., Jackson, J., Walker, R., Reza Gheitanchi, M., & Javad Bolourchi, M. (2006). Strike-slip faulting, rotation, and along-strike elongation in the Kopeh Dagh mountains, NE Iran. *Geophysical Journal International*, *166*(3), 1161–1177. https://doi.org/10.1111/j.1365-246x.2006.02983.x

Huntley, D. J., & Baril, M. (1997). The K content of the K-feldspar being measured in optical dating or in thermoluminescence dating. *Ancient TL*, *15*, 11–13.

Jackson, J., Priestley, K., Allen, M., & Berberian, M. (2002). Active tectonics of the south Caspian basin. *Geophysical Journal International*, *148*(2), 214–245. https://doi.org/10.1046/j.1365-246x.2002.01005.x

Javidfakhr, B., Bellier, O., Shabanian, E., Siame, L., Léanni, L., Bourlès, D., & Ahmadian, S. (2011). Fault kinematics and active tectonics at the southeastern boundary of the eastern Alborz (Abr and Khij fault zones): Geodynamic implications for NNE Iran. *Journal of Geodynamics*, *52*(3–4), 290–303. https://doi.org/10.1016/j.jog.2011.02.005

Khorrami, F., Vernant, P., Masson, F., Nilfouroushan, F., Mousavi, Z., Nankali, H., et al. (2019). An up-to-date crustal deformation map of Iran using integrated campaign-mode and permanent GPS velocities. *Geophysical Journal International*, *217*(2), 832–843. https://doi.org/10.1093/gji/ggz045

Kurtz, R., Klinger, Y., Ferry, M., & Ritz, J. F. (2018). Horizontal surface-slip distribution through several seismic cycles: The Eastern Bogd fault, Gobi-Altai, Mongolia. *Tectonophysics*, *734*, 167–182. https://doi.org/10.1016/j.tecto.2018.03.011

Lyberis, N., & Manby, G. (1999). Oblique to orthogonal convergence across the Turan block in the post-Miocene. *AAPG Bulletin*, *83*(7), 1135–1160. https://doi.org/10.1306/e4fd2e97-1732-11d7-8645000102c1865d

Mattei, M., Cifelli, F., Alimohammadian, H., Rashid, H., Winkler, A., & Sagnotti, L. (2017). Oroclinal bending in the Alborz Mountains (Northern Iran): New constraints on the age of South Caspian subduction and extrusion tectonics. *Gondwana Research*, *42*, 13–28. https://doi.org/10.1016/j.gr.2016.10.003

Mattei, M., Visconti, A. L., Cifelli, F., Nozaem, R., Winkler, A., & Sagnotti, L. (2019). Clockwise paleomagnetic rotations in northeastern Iran: Major implications on recent geodynamic evolution of outer sectors of the Arabia-Eurasia collision zone. *Gondwana Research*, *71*, 194–209. https://doi.org/10.1016/j.gr.2019.01.018

Mosar, J., Kangarli, T., Bochud, M., Glasmacher, U. A., Rast, A., Brunet, M. -F., & Sosson, M. (2010). Cenozoic-recent tectonics and uplift in the Greater Caucasus: A perspective from Azerbaijan. In M. Sosson (Ed.), Sedimentary basin tectonics from the Black Sea and Caucasus to the Arabian platform (Vol. 340, pp. 261–280). Geological Society of London, Special Publication. https://doi.org/10.1144/sp340.12

Mousavi, Z., Pathier, E., Walker, R. T., Walpersdorf, A., Tavakoli, F., Nankali, H., et al. (2015). Interseismic deformation of the Shahroud fault system (NE Iran) from space-borne radar interferometry measurements. *Geophysical Research Letters*, *42*(14), 5753–5761. https://doi.org/10.1002/2015gl064440

Mousavi, Z., Walpersdorf, A., Walker, R. T., Tavakoli, F., Pathier, E., Nankali, H. R. E. A., et al. (2013). Global Positioning System constraints on the active tectonics of NE Iran and the South Caspian region. *Earth and Planetary Science Letters*, *377*, 287–298. https://doi.org/10.1016/j.epsl.2013.07.007

Nemati, M., Hollingsworth, J., Zhan, Z., Bolourchi, M. J., & Talebian, M. (2013). Microseismicity and seismotectonics of the South Caspian Lowlands, NE Iran. *Geophysical Journal International*, *193*(3), 1053–1070. https://doi.org/10.1093/gji/ggs114

Radfar, A., Chakdel, A. R., Nejati, A., & Soleimani, M. (2019). New insights into the structure of the South Caspian Basin from seismic reflection data, Gorgan Plain, Iran. *International Journal of Earth Sciences*, *108*, 379–402. https://doi.org/10.1007/s00531-018-1659-x

Rhodes, E. J. (2015). Dating sediments using potassium feldspar single-grain IRSL: Initial methodological considerations. *Quaternary International*, *362*, 14–22. https://doi.org/10.1016/j.quaint.2014.12.012

Rhodes, E. J., Fanning, P. C., & Holdaway, S. J. (2010). Developments in optically stimulated luminescence age control for geoarchaeological sediments and hearths in western New South Wales, Australia. *Quaternary Geochronology*, *5*, 348–352. https://doi.org/10.1016/j.quageo.2009.04.001

Ritz, J. F., Nazari, H., Ghassemi, A., Salamati, R., Shafei, A., Solaymani, S., & Vernant, P. (2006). Active transtension inside central Alborz: A new insight into northern Iran–southern Caspian geodynamics. *Geology*, *34*(6), 477–480. https://doi.org/10.1130/g22319.1

Rizza, M., Vernant, P., Ritz, J. F., Peyret, M., Nankali, H., Nazari, H., et al. (2013). Morphotectonic and geodetic evidence for a constant slip-rate over the last 45 kyr along the Tabriz fault (Iran). *Geophysical Journal International*, *193*(3), 1083–1094. https://doi.org/10.1093/gji/ggt041

Robert, A. M., Letouzey, J., Kavoosi, M. A., Sherkati, S., Müller, C., Vergés, J., & Aghababaei, A. (2014). Structural evolution of the Kopeh Dagh fold-and-thrust belt (NE Iran) and interactions with the South Caspian Sea Basin and Amu Darya Basin. *Marine and Petroleum Geology*, *57*, 68–87. https://doi.org/10.1016/j.marpetgeo.2014.05.002

Tatar, M., Jackson, J., Hatzfeld, D., & Bergman, E. (2007). The 28 May 2004 Baladeh earthquake (Mw 6.2) in the Alborz, Iran: Overthrusting of the South Caspian Basin margin, partitioning of oblique convergence and the seismic hazard of Tehran. *Geophysical Journal International*, *170*, 249–261. https://doi.org/10.1111/j.1365-246x.2007.03386.x

Tchalenko, J. S. (1975). Seismicity and structure of the Kopet Dagh (Iran, USSR). *Philosophical Transactions of the Royal Society of London - Series A: Mathematical and Physical Sciences*, *278*(1275), 1–28. https://doi.org/10.1098/rsta.1975.0019

Van Dijk, J., Ajayi, A. T., Eid, T., Eldali, M., Ellen, H., Guney, H., et al. (2018). An integrated geological model for the greater Çeleken area central Caspian Basin, Turkmenistan; complex syssedimentary transcurrent faulting and compartmentalization in Plio-Pleistocene clastic reservoirs. In *Abu Dhabi International Petroleum Exhibition & Conference, 12-15 November*. Society of Petroleum Engineers paper SPE-192978-MS.

Vincent, S. J., Morton, A. C., Carter, A., Gibbs, S., & Barabadze, T. G. (2007). Oligocene uplift of the western Greater Caucasus; an effect of initial Arabia-Eurasia collision. *Terra Nova*, *19*(2), 160–166. https://doi.org/10.1111/j.1365-3121.2007.00731.x

Walker, R. T., Bezmenov, Y., Begenjev, G., Carolin, S. A., Dodds, N., Gruetzner, C., et al. (2021). Slip-rate on the Main Kopetdag (Kopeh Dagh) Strike-slip fault, Turkmenistan, and the active tectonics of the South Caspian. *Tectonics*. https://doi.org/10.5281/zenodo.5037978

Walters, R. J., Elliott, J. R., Li, Z., & Parsons, B. (2013). Rapid strain accumulation on the Ashkabad fault (Turkmenistan) from atmosphere-corrected InSAR. *Journal of Geophysical Research: Solid Earth*, *118*(7), 3674–3690. https://doi.org/10.1002/jgrb.50236

Wessel, P., & Smith, W. H. (1995). New version of the generic mapping tools. *Eos, Transactions American Geophysical Union*, *76*(33), 329. https://doi.org/10.1029/95eo00198

Yeats, R. (2012). *Active faults of the world*. Cambridge University Press.

Zinke, R., Dolan, J. F., Rhodes, E. J., Van Dissen, R., & McGuire, C. P. (2017). Highly Variable Latest Pleistocene-Holocene Incremental slip rates on the Awatere Fault at Saxton River, South Island, New Zealand, revealed by Lidar mapping and luminescence dating. *Geophysical Research Letters*, *44*. https://doi.org/10.1002/2017GL075048